

The impact of ram pressure on the radio spectral index and magnetic field of NGC 4522: A high-resolution VLA continuum study

WOORAK CHOI ,^{1,2} AERE CHUNG ,² CHANG-GOO KIM ,³ BUMHYUN LEE ,² LUCA CORTESE ,⁴ TOBY BROWN ,⁵
 BARBARA CATINELLA ,⁴ ERIC Emsellem ,^{6,7} A. FRASER-MCKELVIE ,⁶ JIAYI SUN ,⁸ AND ADAM WATTS 

¹Department of Physics and Astronomy, McMaster University, Hamilton, ON L8S 4M1, Canada

²Department of Astronomy, Yonsei University, 50 Yonsei-ro, Seodaemun-gu, Seoul 03722, Republic of Korea

³Department of Astrophysical Sciences, Princeton University, 4 Ivy Lane, Princeton, NJ 08544, USA

⁴International Centre for Radio Astronomy Research, University of Western Australia, M468, 35 Stirling Highway, Crawley, WA 6009, Australia

⁵Herzberg Astronomy and Astrophysics Research Centre, National Research Council of Canada, 5071 West Saanich Rd, Victoria, BC, V9E 2E7, Canada

⁶European Southern Observatory, Karl-Schwarzschild-Straße 2, Garching, 85748, Germany

⁷Univ Lyon, Univ Lyon1, ENS de Lyon, CNRS, Centre de Recherche Astrophysique de Lyon UMR5574, 69230 Saint-GenisLaval, France

⁸Department of Physics and Astronomy, University of Kentucky, 506 Library Drive, Lexington, KY 40506, USA

ABSTRACT

We present high-resolution Very Large Array (VLA) continuum observations at S-band (3 GHz, 560 pc scale) and X-band (10 GHz, 200 pc scale) of the ram-pressure-stripped Virgo galaxy NGC 4522, to investigate the characteristics of its radio continuum, spectral index, and magnetic field under the influence of the intracluster medium (ICM). The total radio continuum shows an asymmetry that extends northwest, mirroring the H I gas distribution, but showing distinct features in the extraplanar regions. The spectral index steepens systematically from $\alpha \sim -0.6$ in the main disk to $\alpha \sim -1.1$ in the outer disk. We find that the spectral index behavior of the outer disk is mainly due to an ICM shock that can re-accelerate electrons and a significant reduction of thermal emission. Intriguingly, extraplanar clouds exhibit exceptionally flat spectral indices ($\alpha \sim -0.2$ to 0), resulting from a combination of significantly enhanced thermal emission and pronounced spectral aging of the non-thermal component. Although some of these regions correlate with H α , others do not. We propose that the mixing between the ICM and interstellar medium (ISM) is an alternative mechanism that enhances thermal emission independently of star formation. Polarized continuum emissions are highly asymmetric, preferentially distributed along the ICM wind side, and the polarization fraction increases radially outward from the galactic midplane, indicating that the polarized emission is strongly influenced by the ICM wind. Our results show how and where the ICM substantially affects the ISM, and also demonstrate that high-frequency observations are crucial for analyzing the radio continuum of ram pressure stripping galaxies.

Keywords: Galaxies (573) — Galaxy clusters (1772) — Interstellar medium (847) — Radio interferometry (1346) — Radio continuum emission (1340) — Spectral index (1553) — Extragalactic magnetic fields (507)

1. INTRODUCTION

Galaxy clusters represent the densest large-scale environments in the universe, and galaxies near cluster cores tend to be redder and more elliptical than those in cluster outskirts (A. Dressler 1980). Among various environmental mechanisms, ram pressure stripping (RPS), caused by the intracluster medium (ICM), can efficiently remove the interstellar medium (ISM) of galaxies on short timescales, leading to passive galaxy evolution (H. H. Crowl & J. D. P. Kenney 2008).

Email: woorak.c@gmail.com, achung@yonsei.ac.kr

Observations of neutral hydrogen (H I) provide compelling evidence for RPS, revealing truncated and disturbed gas disks as well as gaseous tails in cluster galaxies (e.g., V. Cayatte et al. 1990; A. Chung et al. 2009; M. Ramatsoku et al. 2019; J. Wang et al. 2021). Star formation (SF) in these galaxies is likewise affected, showing both SF suppression due to gas loss (e.g., R. A. Koopmann & J. D. P. Kenney 2004; B. Vulcani et al. 2020a) and localized SF enhancement from gas compression (e.g., A. Abramson et al. 2011; J. D. P. Kenney et al. 2014; B. Vulcani et al. 2020b).

For galaxies undergoing RPS, radio continuum observation, which is a powerful tracer of the magnetized ISM, pro-

vides an especially insightful diagnostic tool. The dominant component of this emission (especially at frequencies below ~ 10 GHz) is typically nonthermal synchrotron radiation (e.g., [I. M. Gioia et al. 1982](#); [J. J. Condon 1992](#); [R. Beck 2001](#)), which arises from cosmic-ray electrons (CRe) spiraling in galactic magnetic fields. Consequently, radio continuum observations provide a direct probe of magnetic field strength and structure. The CRe themselves are primarily accelerated in the supernova remnants, linking the radio emission to the star formation cycle over timescales of ~ 100 Myr. Thermal (free-free) radiation from HII regions ionized by young, massive O/B stars also contributes to the radio continuum at 1 – 10 GHz, typically accounting for ≈ 10 – 40% (e.g., [I. M. Gioia et al. 1982](#); [R. Beck 2001](#); [F. S. Tabatabaei et al. 2017](#)), tracing shorter timescale star formation (~ 10 Myr). Therefore, the total radio continuum is sensitive to both the overall magnetic field strength and star formation activity, while polarized emission particularly traces the ordered magnetic field⁹.

The synchrotron emission spectrum is determined by the energy distribution of CRe, expressed as $j(E) \propto E^s$. The flux density F_ν is related to frequency ν by $F_\nu \propto \nu^\alpha$, where the spectral index α is derived from the CRe spectral slope s via $\alpha = (s + 1)/2$. Since the intrinsic CRe energy spectrum is often approximated by a power-law with a slope of $-3 \lesssim s \lesssim -2$ at $E = 1$ – 10 GeV (e.g., [E. Orlando 2018](#); [M. Padovani et al. 2018](#)), the resulting spectral index, α , generally falls between -0.5 and -1.0 . As CRe propagate through the ISM, they undergo frequency-dependent energy losses ([M. S. Longair 2011](#)), such as synchrotron and inverse Compton losses. High-energy CRe are particularly susceptible to these processes, leading to a systematic steepening of the spectral index. In contrast, thermal (free-free) emission exhibits an almost flat spectral index (≈ -0.1) at frequencies of a few GHz, as expected from its emission mechanism. In general, isolated spiral galaxies exhibit axisymmetric total continuum morphologies with enhanced emission in spiral arm regions, while the strongest polarized emission and well-ordered spiral magnetic field patterns are found in the interarm regions (e.g., [R. Beck 2015](#)). Their spectral indices vary from about -0.5 in star-forming regions within the disk to -1.3 or steeper in the outer regions of galaxies (e.g., [U. Klein et al. 1984](#); [E. Hummel et al. 1991](#); [C. J. Vargas et al. 2018](#)).

The external pressure from the ICM compresses the ISM on the galaxy's leading side, which can enhance magnetic field strengths, potentially triggering bursts of star formation (e.g.,

[H. H. Crowl & J. D. P. Kenney 2006](#); [A. Abramson et al. 2011](#); [B. Vulcani et al. 2018](#)). Meanwhile, in the stripped tail, the radio continuum traces displaced gas, cosmic rays, and magnetic fields as they are pulled away from the galactic disk and interact with the surrounding ICM. Indeed, previous full-polarization radio continuum observations of ram pressure stripped Virgo spirals have revealed strongly asymmetric total emission and enhanced polarized emission along the leading side, with magnetic field vectors oriented roughly perpendicular to the ICM wind direction (e.g., [K. T. Chyží et al. 2007](#); [B. Vollmer et al. 2004, 2007, 2010, 2013](#)). Although these studies revealed that the cluster environment can compress the ISM and order magnetic fields, they found little evidence that ram pressure directly affects the spectral index. Instead, the spectral index appears to be governed primarily by local star-forming activity.

More recently, high-sensitivity low-frequency surveys with LOFAR have significantly expanded the sample of known RPS galaxies. These observations have revealed extended radio tails and complex magnetic field structures not only in massive clusters but also in galaxy groups, demonstrating that nonthermal emission tails are frequent signatures of the stripping process (e.g., [A. Ignesti et al. 2023](#); [I. D. Roberts et al. 2021, 2022, 2024](#)). However, the relatively coarse spatial resolutions (~ 1.5 – 3 kpc) of previous observations have limited our understanding of where, and to what extent, the ICM influences the ISM and its magnetic field in detail. This also hampers detailed multiwavelength comparisons. In addition, separating the thermal emission component has been challenging from MHz to GHz frequencies (144 MHz of LOFAR, 1.4 GHz of L-band, and 5 GHz of C-band) because of the low thermal fraction.

In this paper, we present high-resolution S-band (3 GHz) and X-band (10 GHz) continuum observations of NGC 4522 obtained with the Karl G. Jansky Very Large Array (VLA). These data provide spatial resolutions 2 – 5 times higher than in previous studies. Our multi-band continuum observations enable us to construct detailed spectral index maps, which help disentangle the thermal emission from the dominant nonthermal synchrotron component and address several key questions: Are there signatures of cosmic-ray electron (CRe) re-acceleration driven by ICM shocks? How does the balance between thermal and nonthermal emission vary across the galaxy? How does the ICM influence the galactic magnetic field? Most importantly, where and how does the interaction between the ISM and the hot ICM occur?

This paper is organized as follows. [Section 2](#) describes the target and observations. In [Section 3](#), we present the overall morphology and spectral index distribution of the total continuum. [Section 4](#) focuses on the polarized emission and magnetic field structure. In [Section 5](#), we discuss our results in the context of previous simulations and recent MUSE ob-

⁹ Following the convention in the literature (e.g., [R. Beck 2015](#)), we distinguish between the *total* field, traced by the total continuum, and the *ordered* field, which produces polarized continuum emission. In this paper, we use the term ‘ordered magnetic field’ when discussing the polarized emission in general, and ‘regular magnetic field’ when specifically referring to the large-scale, coherent component.

servations. In this section, we present a schematic overview of our main findings, which highlights the distinct physical processes identified across the galaxy. Finally, we summarize our main findings in Section 6.

2. TARGET AND OBSERVATIONS

2.1. NGC 4522

NGC 4522 is a Virgo Cluster spiral galaxy that shows clear evidence of ongoing H I stripping by ram pressure from the ICM. Basic physical parameters of NGC 4522 are summarized in Table 1. Numerous observational studies have focused on this galaxy, including those based on H I, H α , CO, and radio continuum data (e.g., J. D. P. Kenney et al. 2004; B. Vollmer et al. 2004; B. Lee & A. Chung 2018; A. Boselli et al. 2018), as shown in Figure 1. NGC 4522 is the nearest and clearest example in which multiple gas tracers, including molecular gas, are detected outside the stellar disk. It thus serves as an ideal laboratory to explore how ram pressure influences the multi-phase and magnetized ISM, the coupling among different components, and the stripping conditions that depend on the ISM density.

B. Vollmer et al. 2004 (hereafter V04) observed this galaxy in the L-band (20 cm) and C-band (6 cm) radio continuum at 50 and 15 arcsec resolutions, respectively, revealing an asymmetry similar to that seen in the H I distribution at both frequencies. The C-band polarized continuum emission was also found to be highly asymmetric, predominantly located near the ICM wind front (the eastern side), with its peak offset from that of the total continuum. They further reported that the polarization fraction increases radially outward from the galaxy center and that the spectral index steepens from east to west. However, as noted earlier, their analysis was limited to the global distribution and trends of the (polarized) continuum because of the insufficient spatial resolution. To examine in greater detail how the ISM responds to the external ICM pressure, we have conducted new full-polarization VLA continuum observations of NGC 4522 with significantly improved resolution compared to previous studies.

2.2. High-Resolution VLA Polarized Continuum Observations

We conducted VLA continuum observations of NGC 4522 at 3 GHz (S-band) in February 2020 and at 10 GHz (X-band) in April 2020, with bandwidths of 2 GHz and 4 GHz for the S- and X-bands, respectively, using the C-configuration (Project ID: 20A-310, PI: W. Choi). The full width at half power of the S- and X-bands is 15' and 4.5', respectively, which is sufficiently large to cover the entire stellar disk and extraplanar gas of NGC 4522 (diameter of $\approx 4'$). To achieve a signal-to-noise ratio (SNR) of 3 for polarized emission, on-source integration times of 81 and 280 minutes were used for the S- and X-bands, respectively, assuming a polarization fraction of

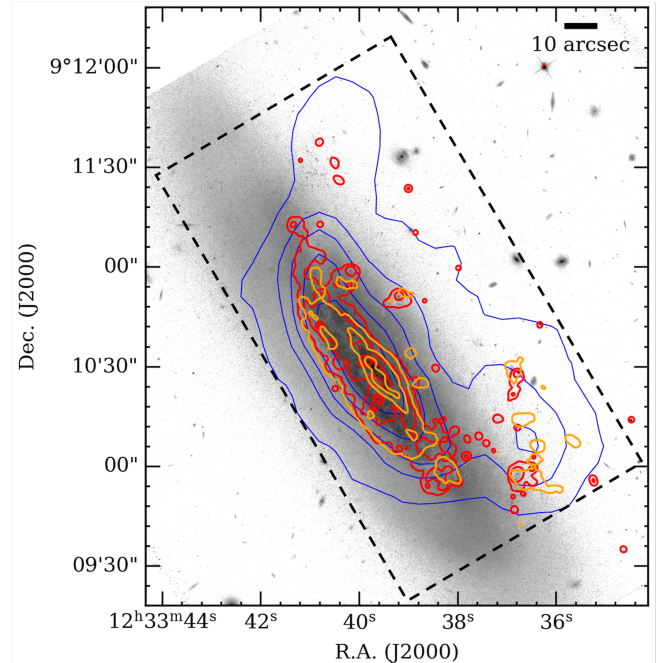


Figure 1. A composite map showing H α (red contours, A. Boselli et al. 2018), ALMA 12CO(1-0) (yellow contours, B. Lee & A. Chung 2018), H I (blue contours, A. Chung et al. 2009), and optical (background, HST WFC F814W) of NGC 4522. This galaxy has a highly asymmetric H I disk with extraplanar molecular gas and associated star-forming regions. The black dashed box indicates the region that is the focus of this study.

Table 1. Basic properties of NGC 4522

Quantity	Value
Type ^a	SBC
R.A. (J2000) ^a	12 ^h 33 ^m 48 ^s .7
Dec. (J2000) ^a	+9°10'30.2"
Distance (Mpc) ^b	16.5
Position Angle (°) ^a	35
Inclination (°) ^a	79
Systemic velocity (km s ⁻¹) ^b	2331
M_{H_I} (M_\odot) ^b	5.64×10^8
M_{H_2} (M_\odot) ^c	3.0×10^8
M_{stellar} (M_\odot) ^d	2×10^9

^a HyperLeda (D. Makarov et al. 2014)

^b A. Chung et al. (2009).

^c B. Vollmer et al. (2008a).

^d L. Cortese et al. (2012).

$\approx 7\%$ at 3 GHz (B. Vollmer et al. 2004, 2013). This ensures a significantly higher SNR for the total continuum emission. To maximize the sensitivity of full-polarization observations, we used an 8-bit sampler for the S-band and a 3-bit sampler for the X-band. 3C 286 was used as the bandpass, flux, and polarization-angle calibrator, and J1239+0730 was used

Table 2. NGC 4522 VLA Observation Parameters

Parameter	S-band (3 GHz)	X-band (10 GHz)
Date of observations	2020 Feb. 18	2020 Apr. 18 – 21
Configuration	C	C
No. of antennas	26	27
No. of spectral windows	16	32
No. of channels per spectral window	64	64
Total no. channels	1024	2048
Channel separation (MHz)	2.0	2.0
Total bandwidth (GHz)	2.024	4.048
On-source time (min)	81	280
Synthesized beam (arcsec) ^a	6.9	2.5
RMS noise ($\mu\text{Jy beam}^{-1}$) ^a	6.0	1.5
Flux calibrator ^b	3C 286	3C 286
Phase calibrator	J1239+0730	J1239+0730
Pol. leakage calibrator	J1407+2827	J1407+2827

^a Briggs weightings of 0.5 and 1.5 were applied to S-band and X-band, respectively.

^b This calibrator was also employed as the bandpass and polarization-angle calibrator.

to calibrate the polarization leakage of the antennas. The observational setup is summarized in Table 2.

The data were initially processed using the pipeline of the COMMON ASTRONOMY SOFTWARE APPLICATIONS PACKAGE (CASA; [J. P. McMullin et al. 2007](#)) 6.4.1 version, provided by NRAO. Additional radio frequency interference (RFI) flagging was manually performed using the task `flagdata`. To obtain both total and polarized continuum data, we followed the standard polarization calibration procedure provided by NRAO. Imaging was performed using the `tclean` task. We generated the mask interactively and cleaned the calibrated data to a depth of twice the root mean square (RMS) noise of the dirty image using this mask. Briggs weighting with robust of 0.5 and 1.5 was applied to the S- and X-band, respectively, during the cleaning process. We also employed the MULTISCALE MULTI-FREQUENCY synthesis (MT-MFS, [U. Rau & T. J. Cornwell 2011](#)) algorithm to improve image quality, taking into account the relatively large bandwidth. Primary beam (PB) corrections are then applied to both bands using the `impbcor` task. The PB correction had a marginal effect, increasing the flux by only up to 1% and 4% at the 4×RMS noise level for the S- and X-bands, respectively, as the extent of our source is sufficiently small compared to the PB in both bands. Finally, we obtained Stokes I, Q, U, and V images for S- and X-bands with synthesized beams of $7\farcs8 \times 6\farcs0$ and $2\farcs8 \times 2\farcs2$ achieving RMS noise levels of $6 \mu\text{Jy beam}^{-1}$ and $1.5 \mu\text{Jy beam}^{-1}$ for S and X-band, respectively. A detailed description of the calibration procedures and continuum imaging is provided in Appendix A.

3. TOTAL CONTINUUM AND SPECTRAL INDEX

3.1. Distribution of Continuum Emission

The total continuum emission at both the S- and X-bands, shown in Figure 2, exhibits a highly asymmetric morphology relative to the stellar disk. The emission is clearly compressed on the southeastern side (bottom of the figure) and extends into a broad tail toward the northwest (top of the figure). This morphology mirrors the stripped H I gas distribution and aligns with the expected direction of the ICM wind, providing clear evidence that the radio continuum-emitting gas responds to ram pressure. At our sensitivity limit, there are regions where S-band emission is detected, but no X-band continuum is observed. The overall morphology of the continuum at these two bands is consistent with that seen in previous C-band (6 cm) observations of this target ([V04](#)).

The overall distributions within the stellar disk are similar across multi-wavelength observations (Figure 2 and 3). At the western edge, where H I is truncated, a sharp truncation is seen not only in the continuum but also in H α ¹⁰ and molecular gas. In contrast, at the eastern edge, H α and molecular gas are less extended than the continuum and H I. The continuum emission is clearly detected in the extraplanar region (upper-right), where H α and molecular gas are present. Interestingly, the continuum in this region at both bands is broadly correlated with H α and molecular gas, although spatial offsets exist between their local peaks. For example, in the northwest, H α and a CO clump are adjacent but only partially overlap, while the continuum extends across both. Moreover, some CO clumps lack corresponding H α but appear associated with local continuum peaks. For reference, the resolutions of the H α ($\approx 3''$) and CO ($\approx 2.3''$) observations are comparable.

We measure the total flux of NGC 4522 to be 12.64 ± 0.41 mJy at S-band and 4.14 ± 0.20 mJy at X-band. We assumed a systematic uncertainty of $\sim 3\%$ on the absolute flux scale for both bands ([R. A. Perley & B. J. Butler 2017](#)), which is accounted for in the spectral index calculation. These values are in good agreement with the overall galaxy spectral energy distribution implied by the L-band (20 cm) flux of 24.3 mJy and the C-band (6 cm) flux of 7.6 mJy reported by [V04](#). These earlier fluxes yield a spectral index of -0.97 . Our S- and X-band fluxes follow the power law extrapolated from the L- and C-band measurements, yielding a consistent spectral index of -0.93 ± 0.05 across the entire L- to X-band range. The spatially-resolved spectral index distributions are further discussed in Section 3.2.

¹⁰ Due to the H α filter of the Canada-France-Hawaii Telescope, this H α data includes a contribution from [N II] line; however, we will refer to it simply as H α .

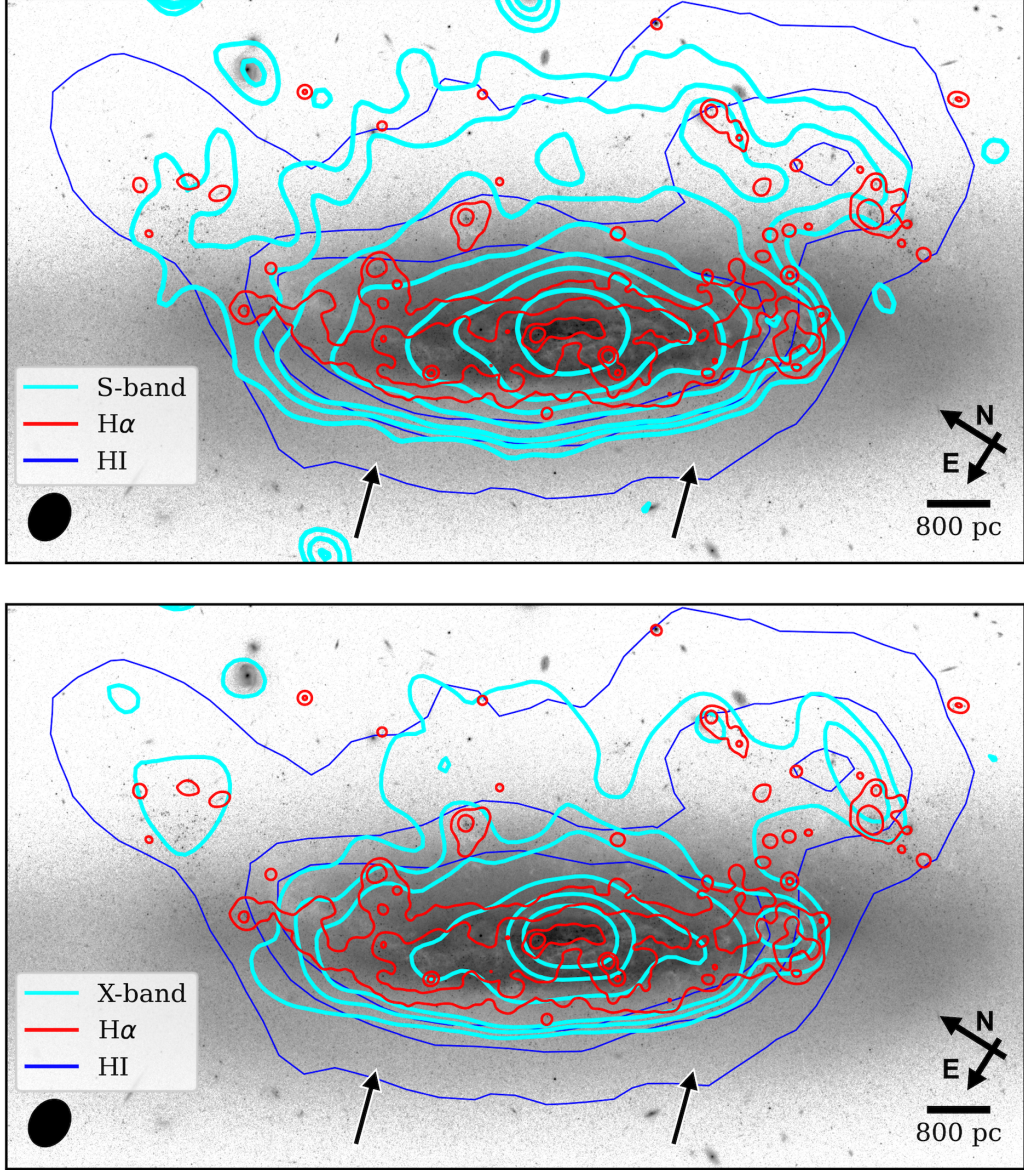


Figure 2. Top: A composite map of S-band total continuum intensity (cyan contours) overlaid with H α (red contours), H I (blue contours), and optical (background, *HST* WFC F814W) of NGC 4522. The contour levels of the S-band continuum are $(4, 7, 10, 20, 35, 50, 90) \times 6 \mu\text{Jy beam}^{-1}$. The synthesized beam of $7''.8 \times 6''.0$ is shown in the bottom-left corner. Compared to the stellar disk, the S-band continuum emission appears asymmetric, extending toward the northwest, similar to the H I gas distribution. **Bottom:** Same as the top panel but for the X-band total continuum convolved to the S-band resolution. The contour levels of the X-band continuum are $(4, 6, 8, 20, 35, 50) \times 5.5 \mu\text{Jy beam}^{-1}$. The convolved synthesized beam of $7''.8 \times 6''.0$ is shown in the bottom-left corner. At this resolution and sensitivity, the X-band continuum is also extended toward the northwest. The expected direction of the ICM wind is indicated by the black arrow.

3.2. Distribution of Spectral Indices

The radio continuum emission at centimeter wavelengths consists of thermal bremsstrahlung (free-free) and nonthermal synchrotron emission. Each component has a distinct spectral index α , which represents the slope of the power-law relation between flux density S and frequency ν ($S \propto \nu^\alpha$). In star-forming galaxies, between 1 and 30 GHz (e.g., J. J. Condon 1992), the nonthermal and thermal components typ-

ically have spectral indices of $\alpha_{\text{NT}} \approx -0.8$ and $\alpha_{\text{T}} \approx -0.1$, respectively. We derive a total spectral index of -0.93 ± 0.05 from the integrated S- and X-band fluxes, indicating that nonthermal emission dominates over this frequency range in NGC 4522. This value is consistent with the result obtained from L- and C-band data by V04 (-0.97) and with the typical indices found in field spiral galaxies (e.g., I. M. Gioia et al. 1982), which also apply to Virgo spirals (e.g.,

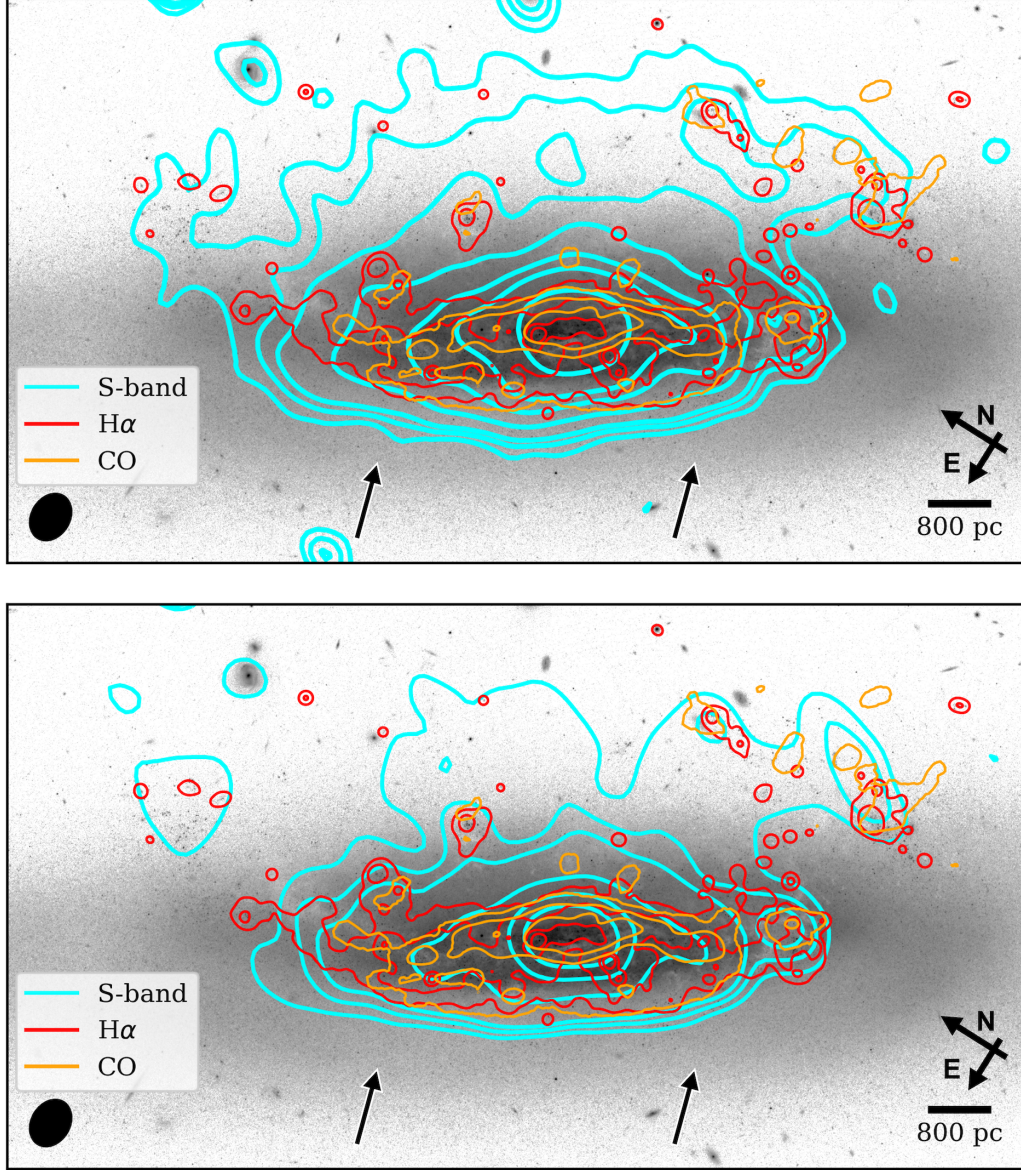


Figure 3. Same as Figure 2, but overlaid with ALMA $^{12}\text{CO}(1-0)$ emission, (yellow contours, B. Lee & A. Chung 2018) instead of H I.

B. Vollmer et al. 2013). However, since the global spectral index is largely dominated by the disk emission, it is therefore necessary to examine its spatial variation to investigate the effects of ram pressure. This is particularly crucial for the extraplanar regions, as the continuum emission there may arise from distinct physical processes.

To generate the spectral index map between S- and X-bands, we first matched the resolution and pixel scale of the two images (as shown in Figure 2 and 3). We then produced the spectral index map using the CASA task `immath` with mode='spix'. Only pixels with convolved X-band emission above $4 \times \sigma_{\text{rms, convol}}$ ($\sigma_{\text{rms, convol}} \approx 5.5 \mu\text{Jy beam}^{-1}$) were included. In Appendix B, we present X-band images generated

with different uv coverages, as well as spectral index maps derived from these images, to assess the effect of convolution. As discussed in Appendix B, we confirm that the convolution process does not affect the robustness of our results.

Figure 4 shows the spectral index map between the S- and X-band. Based on a pixel-by-pixel analysis, we divide the galaxy into four regions: (1) the main disk (within $\text{H}\alpha$ contour; $-0.8 \lesssim \alpha \lesssim -0.5$), (2) the main-disk edges ($R1$ and $R2$), (3) the outer disk (just outside the $\text{H}\alpha$ contour; $-1.1 \lesssim \alpha \lesssim -0.6$), and (4) the extraplanar region ($R3 - R6$ and their vicinity; $-0.6 \lesssim \alpha \lesssim 0$).

Across the main disk (defined by the $\text{H}\alpha$ contour), the spectral index gradually steepens from the galactic center

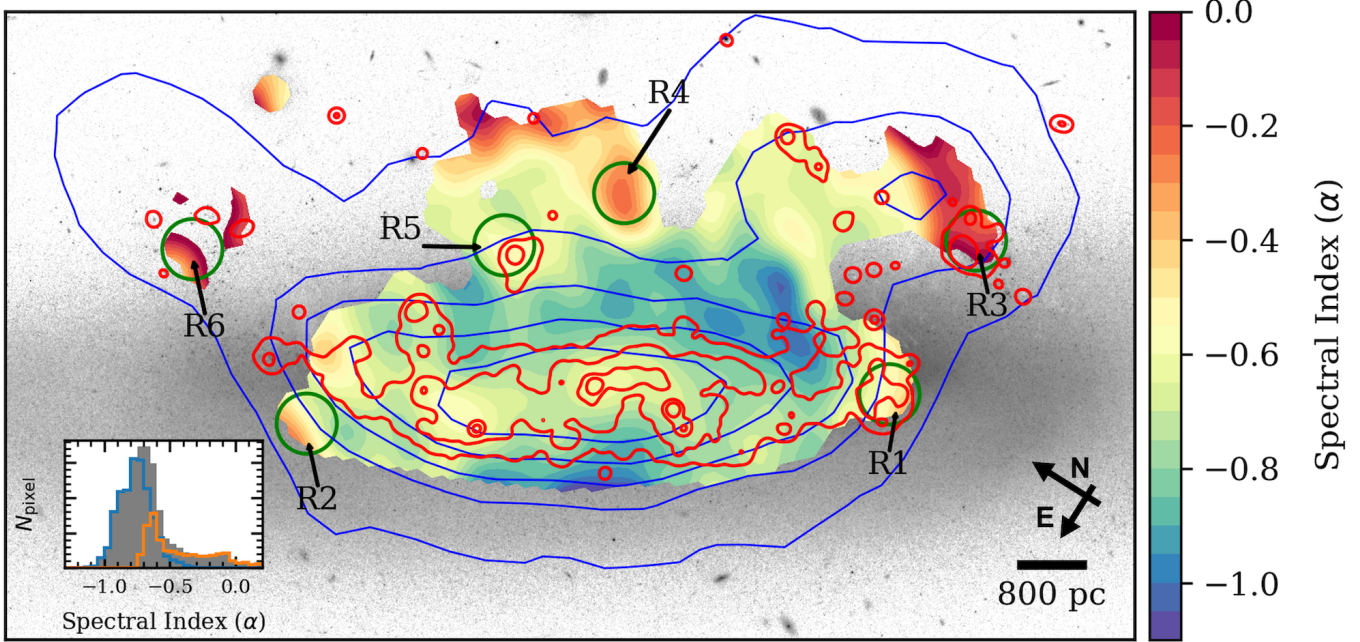


Figure 4. Spectral index map between the S-band and X-band total continuum. H I and H α are shown as blue and red contours, respectively. Only pixels where the convolved X-band emission exceeds $4 \times \sigma_{\text{rms, convol}}$ ($\sigma_{\text{rms, convol}} \approx 5.5 \mu\text{Jy beam}^{-1}$) are displayed. Six regions of interest (R1 – R6) are indicated by green circles. The spectral index generally steepens from the midplane to large scale heights, but increases again in the extraplanar regions, where very complex variations and extremely flat spectral indices are observed. The inset shows the spectral index distribution, with orange and blue histograms representing the extraplanar region (R3 – R6 and their vicinity) and the rest of the galaxy, respectively. Overall, the spectral index is slightly flatter (−1.2 to 0.1) than that reported by V04 from L- and C-band data (−2 to −0.7).

toward the outskirts, with typical values ranging from $\alpha \approx -0.8$ to -0.5 . Regions showing relatively flat spectral indices (−0.6 to −0.5) generally coincide with areas of bright H α emission.

The main disk edges (R1 and R2), where H I is truncated by RPS, tend to show a flattening of the spectral index from −0.6 to −0.3. The flattening in R1 is likely due to a nearby strong H α region that enhances the thermal emission contribution, whereas no prominent H α is found in R2. Enhanced ICM-ISM interactions along the disk edges may also contribute to the spectral flattening, as discussed further in Section 5.

The outer disk, defined as the region outside the outermost H α contour but still within the stellar disk, shows a noticeably steeper spectral index than the main disk, with typical values of $\alpha \approx -1.1$ to -0.6 . This region can be divided into two parts: the leading side, which corresponds to the near side of the outer disk (A. Abramson & J. D. P. Kenney 2014) where the ICM wind compressed the continuum and H I, and the northern region, corresponding to the far side of the outer disk. Hereafter, we refer to this northern region as the ‘far side’. However, due to the high inclination of the galaxy, the emission observed in this region is likely a superposition of the far side of the outer disk and the stripped gas located at the near side (specifically, trailing gases projected along the line-of-sight). Consequently, the observed continuum here includes contributions from these near side stripped

components, which are also likely to interact with the ICM wind. The steepening on the leading side mainly appears in the middle of the galaxy, whereas on the far side it is more widespread.

Most strikingly, the spectral index significantly flattens in the extraplanar region, displaying a complex mixture of structures and variations. While some regions show spectral indices comparable to those of the main disk (e.g., R5, −0.7 to −0.5), others exhibit exceptionally flat spectral values (e.g., R3, R4, R6, −0.3 to 0). Among these regions, H α emission is detected in R3 and R5, whereas it is nearly absent in R4 and R6. To our knowledge, such flat spectral indices have not been reported in previous continuum observations of RPS galaxies, particularly in extraplanar regions. The origin of these unusually flat spectra, especially in areas lacking clear signs of star formation, suggests the presence of complex physical processes, which we discuss in detail in Section 5.

Compared to the spectral index map of V04, our results show a similar trend within the stellar disk, namely, a gradual steepening of the spectral index toward the outer disk. However, the overall spectral indices in our map are systematically flatter (−1.1 to 0) than those reported by V04 (−2 to −0.6). In addition, our high-resolution spectral index map reveals several intriguing features that were not identified in V04: (1) a steepening in the outer disk followed by a flattening in the extraplanar region, (2) a very steep spectral index on the

leading side, and (3) locally flattened spectral indices along the main disk edges. We note that all of these newly detected features arise from differences in both spatial resolution and observing frequency.

4. POLARIZED CONTINUUM EMISSION

In this section, we present new high-resolution S-band and X-band polarization maps of NGC 4522 to investigate in detail how the ICM wind shapes the galactic magnetic field. The polarized intensity, P , and the polarization angle, χ , were derived from the Stokes Q and U maps, which were generated using the same imaging parameters as the total-intensity maps. We then constructed the polarized intensity and polarization angle maps as $P = \sqrt{Q^2 + U^2}$ and $\chi = (1/2) \arctan(U/Q)$.

4.1. General Properties of the Polarized Emission

Figure 5 shows the polarized continuum emission (magenta contours) and the apparent magnetic field vectors (yellow pseudo-vectors) of NGC 4522 at S-band (top panel) and X-band (bottom panel). The total-intensity map at X-band in this figure is shown at its native resolution ($2''.8 \times 2''.2$). The pseudo-vectors are rotated by 90 degrees, such that they indicate the orientation of the ordered magnetic field, as the observed linear polarization traces the electric field, which is perpendicular to the magnetic field. We note again that no Faraday rotation correction has been applied to either band.

NGC 4522 exhibits highly asymmetric and localized polarized emission across the galaxy. In the S-band, most of the polarized emissions is distributed along the northeastern edge of the main disk (i.e., the leading side), with local peaks displaced from the total continuum distribution (i.e., galactic midplane). Although noisier, the X-band polarized emission shows similar overall distribution along the leading side, with its peak also offset from the total continuum peak toward the leading edge. Despite this shared large-scale asymmetry, the detailed distributions of polarized emission differ between the two bands: the S-band reveals faint emission near the galactic center and in the outer disk, whereas the X-band emission is absent at the center but more concentrated around it. These characteristics stand in stark contrast to those of normal spiral galaxies, where polarization emission typically shows a symmetric pattern (see R. Beck 2015 for a compilation of 6 cm observations).

In both bands, most of the polarized emissions do not coincide with optical galactic structures such as dust lanes or star-forming regions (see A. Abramson et al. 2016), but instead appear in the outer disk region. Moreover, although both H I and the total continuum clearly show that the ram pressure affects both the eastern and western sides of the ISM disk, it is unusual that polarized emission is detected only on one side (B. Vollmer et al. 2007, 2013). The enhanced and

extended polarized emission toward the northeast is unlikely caused by an increased CRe density and/or magnetic field amplification due to compression, since the total continuum is not significantly enhanced in this region but merely shows compressed structures.

Meanwhile, V04 reported that the flattest region of the spectral index coincides with the C-band polarized emission, but not with the H α or C-band total continuum peak. They suggested that this may result from a large-scale shock producing the polarized emission at the leading side. However, our observations reveal a clear offset between the peak of the S-band (or X-band) polarized emission and the flattest region of the spectral index. This discrepancy is likely due to the higher angular resolution of our data. The measured offset is less than 15 arcsec, which could not have been distinguished in the previous observations with a resolution of 20 arcsec. Alternatively, the difference may arise from the flux excesses in our X-band continuum data, leading to a slightly different spectral index distribution.

The overall magnetic field in the S-band appears slightly tilted with respect to the major axis of the galactic disk near the ICM wind front and gradually rotates clockwise toward the north. Near the galactic center, some magnetic field vectors are oriented nearly perpendicular to the major axis. The magnetic field direction in the S-band shows an abrupt flip from approximately $-70 \sim -80$ degrees near the peak of the polarized emission to $+70 \sim +80$ degrees farther north, although this may be due to the 180 degree ambiguity inherent in polarization angles. The overall magnetic field morphology is consistent with that reported by V04, which also showed a magnetic field roughly parallel to the galactic disk with a slight bending toward the north.

The magnetic field in the X-band appears more coherent than that in the S-band. It is nearly parallel to the galactic disk, with orientations ranging from approximately -40 to -55 , regardless of location. Considering that the Faraday rotation is negligible at X-band frequencies (R. Beck 2015; see also Section 4.3), the X-band magnetic field directions are more reliable than those in the S-band. Our observations show only weak polarized emission and magnetic field signals in the extraplanar regions, indicating a lack of a well-aligned magnetic field there.

4.2. Polarization Fraction

As the polarized emission traces the ordered magnetic field, the polarization fraction ($p \equiv P/I$), defined as the ratio of polarized intensity to the total radio continuum intensity, can therefore be used to estimate the degree of magnetic field uniformity. The intrinsic polarization fraction p_0 of synchrotron emission in a perfectly ordered field is given by $p_0 = (1 - \alpha)/(5/3 - \alpha)$ (R. Beck 2015), yielding values of 60 – 75% for α of $-0.5 \sim -1.0$. However, the observed po-

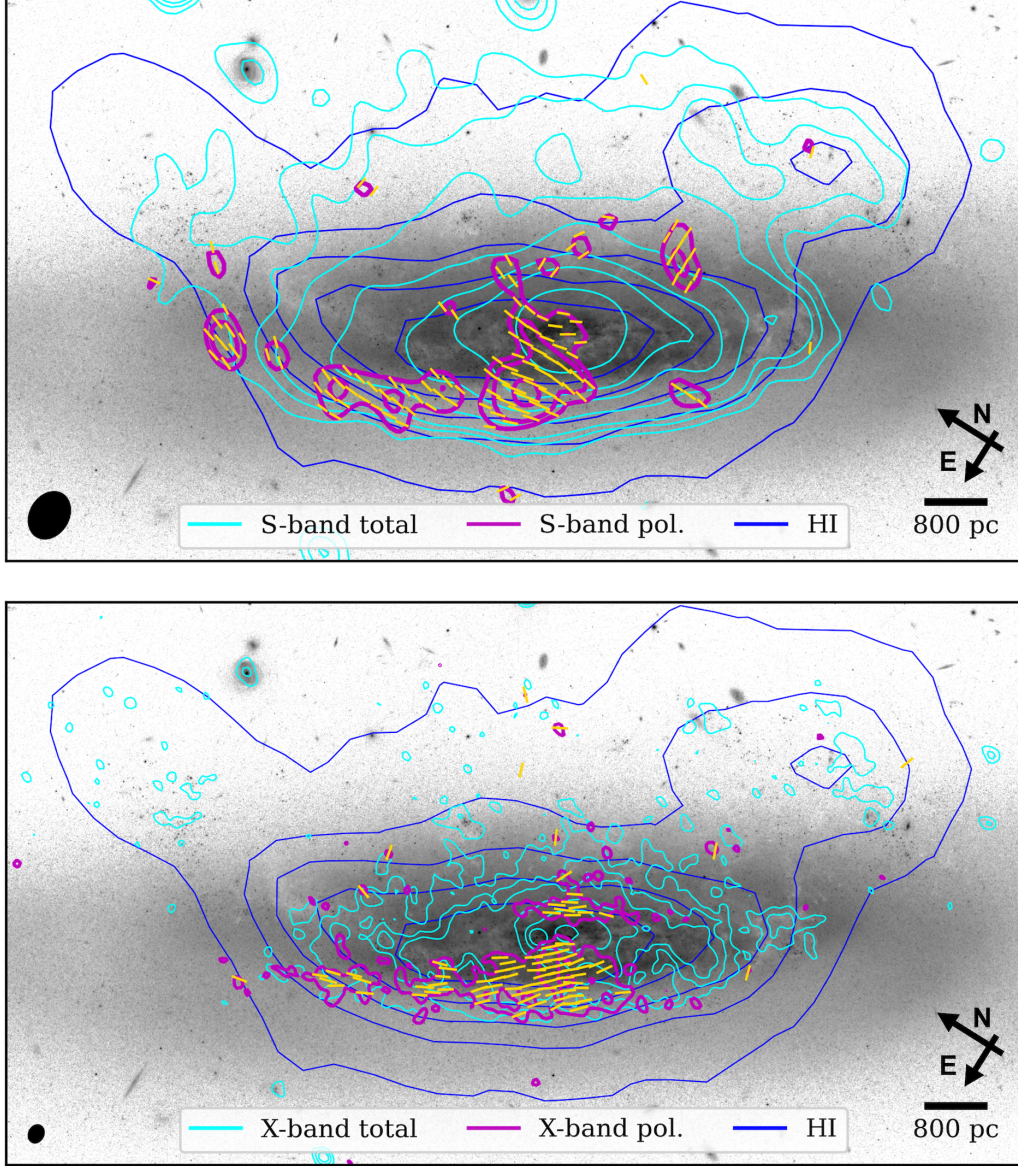


Figure 5. **Top:** S-band polarized continuum intensity (magenta contours) and apparent magnetic field vectors (yellow pseudo-vectors, uncorrected for Faraday rotation) overlaid on the optical image. Blue and cyan contours represent H I and the S-band total continuum, respectively. The contour levels of the polarized emission are $(3.5, 4.5, 7) \times 6 \mu\text{Jy beam}^{-1}$. Polarized emission is highly asymmetric and mainly concentrated near the ICM wind front (southeast region). The polarization angles are roughly parallel to the galactic disk in this area. **Bottom:** Same as the top panel but for the X-band. The contour levels of the polarized emission are $(4, 7) \times 1.5 \mu\text{Jy beam}^{-1}$. As in the S-band, X-band polarized emission also appears near the ICM wind front and extends toward the northeast. The magnetic field vectors are nearly parallel to the H I distribution, suggesting that the ISM in this region is strongly influenced by the ICM. Note that the X-band total-intensity map in this panel is shown at its native resolution ($2''.8 \times 2''.2$).

larization fraction is generally smaller than p_0 due to thermal emission and Faraday depolarization (R. Beck 2015). In unperturbed spiral galaxies, the polarization fraction is typically higher in the interarm than along the spiral arms and shows a symmetric distribution with increasing values toward the outer disk (R. Beck 2005, and references therein), ranging from 10 to 40% in C-band (6 GHz) observations (M. Krause

et al. 2020). In our case, we expect a higher polarization fraction in the outer disk, particularly on the leading side, than in normal spiral galaxies, since polarized emission can be enhanced by ISM compression and/or shear motions induced by the ICM, or magnetic draping (C. Pfrommer & L. Jonathan Dursi 2010).

Figure 6 presents the polarization fraction maps of the S-band (top) and X-band (bottom). From the pixel-by-pixel analysis, the polarization fraction in the S-band ranges from 0 to 80%, with an intensity-weighted mean of $\approx 22\%$. The X-band shows a range, from 10 to 100%, with an intensity-weighted mean of $\approx 48\%$. When derived from the integrated total and polarized continuum intensities, the global polarization fractions are 12% and 41% for the S- and X-bands, respectively. The polarization fraction increases gradually from the galactic center to the outer disk and also rises toward the northeast direction. This trend closely matches that reported by V04, who found that the C-band polarization fraction increases from west to east, reaching its maximum in the northeast region.

The localized polarized emission and high polarization fraction on the ICM wind front (northeastern direction) imply that RPS is responsible for enhancing the ordered magnetic field potentially via large-scale compression/stretching of the galaxy's field or magnetic draping. This aligns with previous studies that have also observed an enhanced polarization fraction on the leading side of RPS galaxies (e.g., H. H. Crowl et al. 2005; B. Vollmer et al. 2008b, 2013)

As shown in the Figure 6, the overall polarization fraction is higher in the X-band than in the S-band. Since Faraday depolarization is proportional to the square of the wavelength ($\propto \lambda^2$), the S-band continuum suffers stronger Faraday depolarization than the X-band. This can therefore be a major cause of the lower polarization fraction in the S-band. Meanwhile, we suggest that thermal continuum emission is enhanced near the H I truncation radius and the extraplanar region based on the flat spectral indices in Figure 4. The enhancement of thermal continuum emission may account for the non-detection of polarized emission in these regions and some regions within the stellar disk. However, because the thermal emission has a flat spectrum, the overall difference in the polarization fraction between the S-band and X-band is not due to the enhanced thermal contribution.

4.3. Rotation Measure and Magnetic Field Strength

The polarization angle is rotated as the emission propagates through a magnetized medium, a phenomenon known as Faraday rotation. The change in the polarization angle ($\Delta\Psi$) depends on the observed wavelength (λ) and the rotation measure (RM) according to the following relation:

$$\Delta\Psi = \text{RM} \times \lambda^2, \quad (1)$$

where $\Delta\Psi = \chi - \chi_0$ represents the change in the polarization angle, χ and χ_0 are the observed and intrinsic polarization angles, respectively, and λ is the wavelength in meters. RM is proportional to the line-of-sight component of the magnetic field (B_{\parallel} , in μG) and the electron density (n_e , in cm^{-3}),

$$\text{RM} = 0.812 \int n_e B_{\parallel} dl. \quad (2)$$

Thus, by assuming reasonable values for the electron density and the path length (dl), we can estimate the strength of the line-of-sight magnetic field.

Since the intrinsic polarization angle is unknown, we derived the RM from the difference in the observed polarization angles between the S-band and X-band. While RM synthesis analysis (e.g., M. A. Brentjens & A. G. de Bruyn 2005) is ideal for disentangling multiple emitting sources along the line-of-sight, our dataset lacks the wide λ^2 coverage required to achieve sufficient resolution in Faraday depth space. Therefore, we derive the RM assuming a simple foreground screen model, calculating it as $\Delta(\Delta\Psi) = \text{RM} \times (\lambda_{\text{s-band}}^2 - \lambda_{\text{x-band}}^2)$. To calculate $\Delta(\Delta\Psi)$, we matched the resolution and pixel scale of the two bands by convolving the X-band Stokes Q and U maps to the synthesized beam of the S-band and then regridding them to the same pixel size. We then generated polarization angle vectors from the convolved Stokes Q and U maps. The differences between the original and convolved X-band polarization angles are typically less than 10 degrees, and we clipped all pixels below four times the rms noise of the convolved X-band map ($\sigma_{\text{rms, convol}} \approx 5.5 \mu\text{Jy beam}^{-1}$).

The top panel of Figure 7 shows the RM map derived from the S-band and X-band data, overlaid with H I, H α , and S-band total continuum emission on the optical image. RM values range from -100 to 350 rad m^{-2} , clustering mainly around two ranges $-100 - 0 \text{ rad m}^{-2}$ (bluish regions) and $200 - 300 \text{ rad m}^{-2}$ (orange regions). These absolute values are slightly higher than those typically found in external galaxies - $|\text{RM}| \lesssim 150 \text{ rad m}^{-2}$ (U. Klein & A. Fletcher 2015, and references therein). Due to large variations in polarization angle seen in the S-band (Figure 5), RM also shows strong spatial variations near the ICM wind front and around the galactic center. According to the definition of RM, these sign reversals (from positive to negative and vice versa) imply reversals of the line-of-sight magnetic field between those regions.

We assessed the potential contribution of foreground Faraday rotation from both the Milky Way and the Virgo cluster ICM. The Galactic contribution in the direction of NGC 4522 is estimated to be less than 20 rad m^{-2} (A. R. Taylor et al. 2009). This value is an order of magnitude smaller than the RM variations observed in NGC 4522 (up to $\sim 300 \text{ rad m}^{-2}$). Regarding the ICM, previous studies have revealed that the RM reaches 10 rad m^{-2} in Virgo Cluster (e.g., J. P. Vallee 1990), which is also much smaller than that of NGC 4522. Therefore, we did not apply any correction for the foreground media, as it does not affect our interpretation of the RM gradients and magnetic field orientations.

The bottom panel of Figure 7 shows the electron-density-weighted magnetic field strength along the line-of-sight

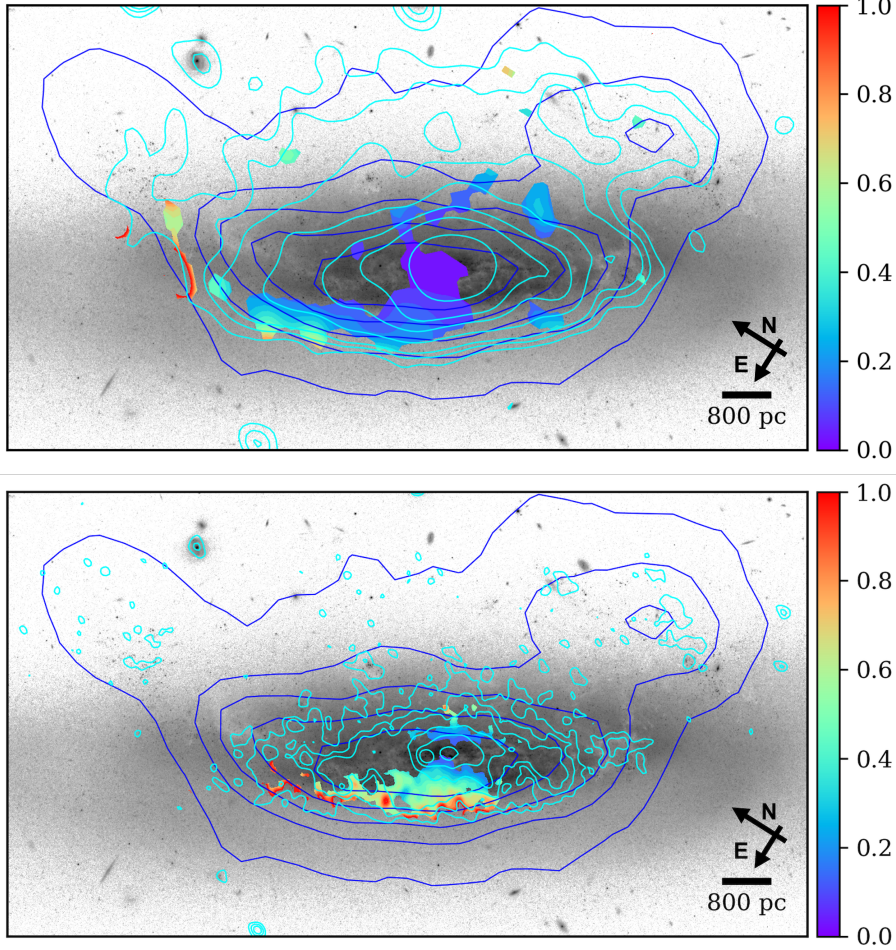


Figure 6. Top: S-band polarization fraction map. Blue and cyan contours represent H I and the S-band total continuum, respectively. The polarization fraction is generally low ($\lesssim 10\%$), but increases gradually outward the outer regions, reaching its highest values near the ICM wind front. **Bottom:** Same as the top panel but for the X-band. The polarization fraction is very low near the galactic center and gradually increases outward. The distribution is roughly axisymmetric, with a few localized polarized regions in the northwest part of the galaxy.

$(B_{\parallel,\text{avg}})$, derived by inverting Equation 2, i.e.,

$$B_{\parallel,\text{avg}} \equiv \frac{\text{RM}}{0.812N_e} \approx \frac{\text{RM}}{0.812N_{\text{H I}}x_e}. \quad (3)$$

Here, $N_e \approx N_{\text{H I}}x_e$ represents the electron column density, neglecting the contribution from fully ionized gas. This approximation is reasonable for the leading side of the disk, where polarization emission is strong, since these regions lie outside the $\text{H}\alpha$ contour. To construct this map, we adopt the H I column density of NGC 4522 from [A. Chung et al. \(2009\)](#) and assume a typical electron fraction in the warm neutral medium, $x_e \sim 0.1$ (e.g., [N. B. Linzer et al. 2024](#)).

As a result, the strength of $|B_{\parallel}|$ ranges from 0 – 15 μG with a median value of $\approx 6 \mu\text{G}$. Regions with large RM values (e.g., the outer disk) tend to exhibit stronger magnetic fields than those with small RM values (e.g., the galactic center). The values of $|B_{\parallel}|$ are comparable to typical magnetic field strength of normal spiral galaxies (10 – 15 μG , [R. Beck 2015](#)). However, the distribution of magnetic field strength

within NGC 4522 remain inconclusive, as the current results only reflect the ordered, line-of-sight component of the total magnetic field.

We note that the electron fraction is likely higher than 0.1 inside the $\text{H}\alpha$ contour due to the presence of ionized gas. Therefore, the $|B_{\parallel}|$ values within the $\text{H}\alpha$ -emitting region in [Figure 7](#) should be regarded as upper limits. We also emphasize that this estimate is simplified, as it assumes no correlation between $|B_{\parallel}|$ and n_e . However, such a correlation may exist in reality; thus independent observations and direct measurements of n_e are required for a more accurate determination of $|B_{\parallel}|$.

5. DISCUSSION

5.1. Possible Origins of Complex Spectral Indices

We observe systematic variations in the spectral index, characterized by $\alpha \sim -0.6$ in the main disk (enclosed by the innermost H I and $\text{H}\alpha$ contours), which steepens to $\alpha \sim -1$ in

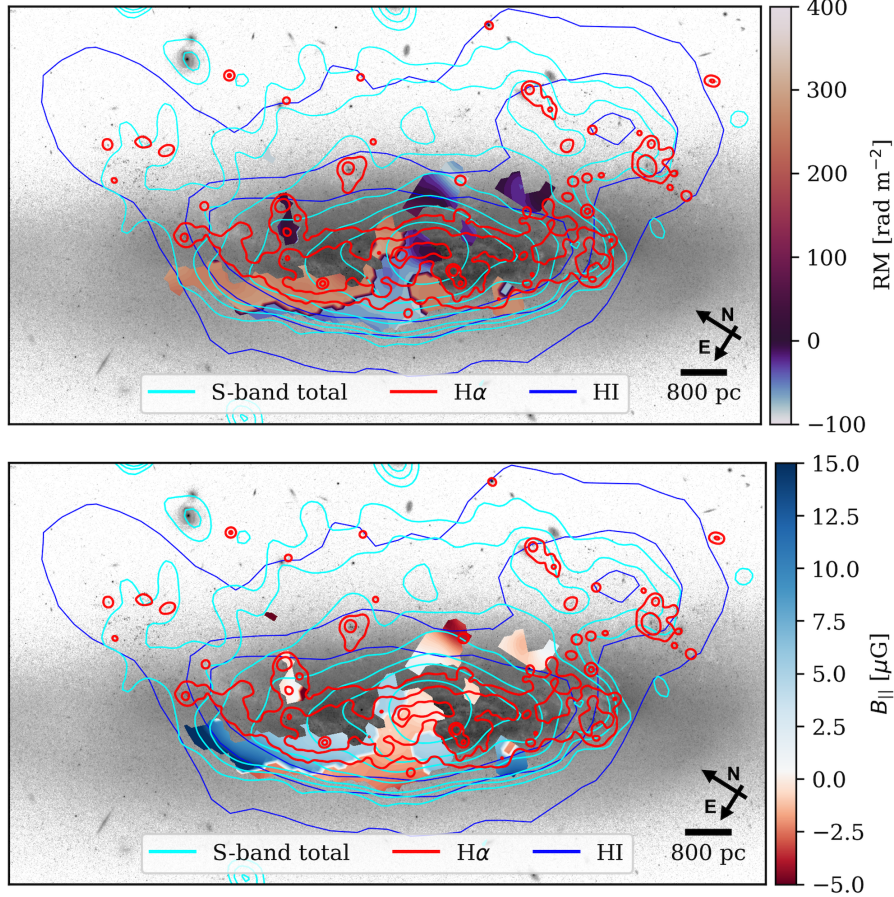


Figure 7. Top: A map of the rotation measure between the S-band and X-band, shown using a cyclic color scale. **Bottom:** A map of the line-of-sight magnetic field strength derived from Equation 2, shown with a red-blue color scale. In both panels, the blue, cyan, and red contours represent H I, the S-band total continuum, and H α , respectively.

the outer disk and then significantly flattens to $\alpha \sim 0$ in the ram-pressure-stripped gas and clouds. A gradual steepening of the spectral index away from the main disk is commonly observed in other galaxies and is often interpreted in the context of CRe aging. For example, C. J. Vargas et al. (2018) observed a sample of edge-on galaxies in the L (1.5 GHz) and C (6 GHz) bands, decomposing the total radio emission into the thermal and nonthermal components by estimating the thermal fraction from the star formation rate inferred from H α . They concluded that the outward steepening is primarily due to energy losses of CRe as they propagate away from their acceleration sites (J. J. Condon 1992). In addition, because the thermal contribution near the midplane is generally higher, the steepening of the total emission with increasing height is more pronounced than that of the nonthermal component alone.

To interpret the spectral index variations across NGC 4522, we employed a simple two-component model. The total flux density S_ν at each frequency ν was modeled as the sum of thermal and nonthermal component, $S_\nu = S_{\nu,\text{th}} + S_{\nu,\text{nt}}$. The thermal emission is represented by a power law with a fixed

spectral index of $\alpha_{\text{th}} = -0.1$ ($S_{\nu,\text{th}} \propto \nu^{-0.1}$). The nonthermal emission was also modeled as a power law, $S_{\nu,\text{nt}} \propto \nu^{\alpha_{\text{nt}}}$, but both its spectral index α_{nt} and normalization were treated as free parameters. We note that modeling the nonthermal emission as a single power law is an approximation, as an aged CRe population is physically expected to exhibit a curved radio spectrum due to energy losses, potentially introducing uncertainties in regions dominated by CRe aging.

The possible outcomes of the interplay between these two components are illustrated in Figure 8. Depending on the relative contributions of each component and the degree of CRe aging, which steepens α_{nt} , the observed spectrum may appear steep, flat, or curved. For instance, in the main disk, we generally expect a larger fraction of nonthermal emission compared to the thermal component within the frequency range of interest (top left). If CRe aging occurs, typically found in the outer regions of galaxies (e.g., C. J. Vargas et al. 2018; V. Heesen et al. 2019; M. Stein et al. 2023), the higher-frequency nonthermal emission is suppressed, resulting in a steeper spectral index (top right). When the free-free emission is significantly reduced, a purely nonthermal spectrum emerges (bottom left).

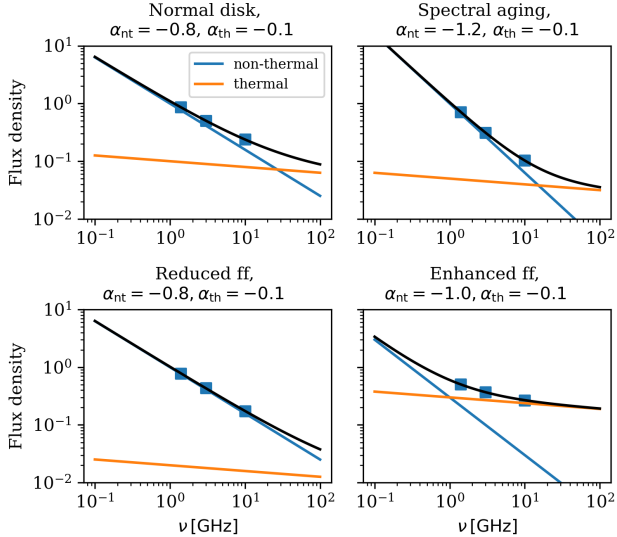


Figure 8. Schematic diagram illustrating four different cases of the two-component radio continuum. The total continuum (black curve) is composed of synchrotron (blue line) and free-free (orange line) emissions. The blue squares indicate the three data points used to constrain the three free parameters of the model. **Top left:** The nonthermal emission dominates over the thermal emission at all frequencies, as typically expected in the main disk. **Top right:** A steeper spectral index results from the reduced high-frequency nonthermal emission (i.e., CRe aging), commonly seen in outer regions. **Bottom left:** Purely nonthermal spectrum caused by a significant reduction of thermal emission. **Bottom right:** Flattened spectral index due to enhanced thermal emission.

Conversely, if the thermal emission dominates over the synchrotron component, the resulting spectral index becomes flatter (bottom right).

To perform this fitting, we incorporated archival lower-resolution L-band (1.4 GHz) continuum observations from [A. Chung et al. 2009](#) (~ 14 arcsec of synthesized beam) and NRAO VLA Sky Survey (45 arcsec of synthesized beam, [J. J. Condon et al. 1998](#)), together with our data. We ran the CASA task `feather` to combine two L-band continuum images, which help to recover more of the faint extended emission. The S- and X-band maps were convolved and re-projected to match the resolution and pixel grid of the L-band map. The top panel of [Figure 9](#) shows the L-band continuum intensity map, with the regions used for our analysis indicated by black dotted boxes. This three-bands approach enables a direct decomposition of the radio continuum by simultaneously solving for the three free parameters: thermal flux, nonthermal flux, and α_{nt} . We note that this method provides a more robust decomposition than those based on $\text{H}\alpha$ scaling, especially facilitated by our 10 GHz data, where the thermal contribution becomes significant.

The bottom panels of [Figure 9](#) show the results of two-component fits for the regions of interest. Note that the spec-

tral indices between the convolved S- and X-band images are slightly different from those in [Figure 4](#) due to additional convolution, although the overall trend remains consistent. The main disk exhibits a typical combination of nonthermal and thermal components, with a thermal fraction of $\approx 14\%$ at 1.4 GHz, consistent with that of nearby galaxies at the same frequency (e.g., [J. J. Condon 1992](#); [F. S. Tabatabaei et al. 2017](#)). At the X-band (10 GHz), the thermal fraction is considerably higher, exceeding the nonthermal contribution. This value is significantly higher than that typically found in nearby galaxies, where the mean thermal fraction is reported to be around 23% at a comparable frequency of 5 GHz ([F. S. Tabatabaei et al. 2017](#)).

In the outer disk (both the leading and far sides), the emission is dominated by nonthermal emission with α_{nt} of $-0.8 \sim -0.9$ which is flatter compared to the main disk. On the leading side, the galaxy likely experiences a supersonic encounter with the ICM. Considering the relative velocity of NGC 4522 to the ICM ($\sim 1500 - 3000 \text{ km s}^{-1}$) and the sound speed of the ICM ($c_{s,\text{ICM}}$), the estimated Mach number is $\mathcal{M} \sim 2 - 3$, implying the formation of a global bow shock encompassing the galaxy. In the downstream of the bow shock, the ICM is thermalized and slows down to the speed subsonic compared to $c_{s,\text{ICM}}$. However, the postshock velocity remains highly supersonic with respect to the cold and warm ISM ($c_{s,\text{ISM}} \approx 1 - 10 \text{ km/s} \ll c_{s,\text{ICM}}$).

Consequently, local shocks are likely driven into the ISM at the interfaces, re-accelerating CRe and enhancing the nonthermal emission. On the far side, although significant spectral aging is expected given its distance from the galactic midplane, clear evidence of such aging is barely visible. This region also exhibits a spectral shape close to a pure power-law that is slightly flatter than that of the main disk, similar to the leading edge. Given the galaxy's high inclination and the 3D geometry of the interaction between the ICM and the galaxy ([B. Vollmer et al. 2006](#)), the global bow shock and the postshock flow envelop the galactic disk rather than being confined to the immediate leading side. Thus, the far side is also subject to these local shocks driven by the interactions between the ICM and the ISM, where CRe aging is mitigated by re-acceleration and/or the injection of fresh CRe.

This interpretation is consistent with the high $[\text{S II}]/\text{H}\alpha$ ratios (indicating shock-excited gas) observed in these regions (see [Section 5.3](#)). Furthermore, the derived spectral index (≈ -0.8) is broadly consistent with that of radio continuum emission at cluster merger shocks, such as those observed in the merging cluster Abell 3411-3412, where electron re-acceleration also occurs ([R. J. van Weeren et al. 2017](#)). We note that while the leading side, where localized polarized emission is observed, likely experiences magnetic draping, this mechanism alone cannot explain the flattened nonthermal spectral index. An enhanced magnetic field acceler-

ates synchrotron cooling ($t_{\text{cool,syn}} \propto B^{-2}$), which would lead to even steeper spectral indices. At the same time, it leads us to observe electrons with lower energy at a fixed observing frequency ($E \propto B^{-0.5}$; e.g., [M. Padovani et al. 2021](#)), which could potentially result in a flatter spectral index, especially if the emission originates from an aged CRe population. Consequently, the net impact of magnetic draping on the spectral index remains inconclusive due to the complex interplay between accelerated synchrotron cooling and the shift in the sampled electron energy range.

The stripped clouds (R3 and R4) exhibit a dominance of thermal emission at higher frequencies and a very steep non-thermal spectral index, indicating strong CRe aging. The inferred thermal emission levels are higher than those in the outer disk. These results highlight the need for an additional source of thermal emission in the extraplanar region. It should be noted that, owing to the shallower sensitivity of the L-band continuum observation compared to the S- and X-band data, only two regions were analyzed.

Meanwhile, the slope between the L- and S-bands (green dotted line) steepens from -0.98 to ≈ -1.3 between the main disk and the extraplanar region, whereas the slope between the S- and X-bands (blue dotted line) flattens from -0.73 to ≈ -0.5 . This difference explains why our spectral index variations differ from those reported by [V04](#) and underscores the importance of high-frequency bands (e.g., X-band), which can more reliably trace thermal contribution in the continuum analysis of RPS galaxies.

We now focus on the pronounced flattening of the spectral index observed in the ram-pressure-stripped clouds. In particular, R3 and R6 exhibit spectral indices of $\alpha \sim 0$, which can only be explained by a complete dominance of thermal emission, as shown in [Figure 9](#). This implies that either the thermal emission is strongly enhanced or the nonthermal emission is significantly suppressed. What could cause such a relative enhancement of thermal emission? Recently formed, young and massive stars emit copious ionizing radiation that creates ionized regions with high electron densities, producing strong free-free emission. Consequently, a flatter radio spectrum is naturally expected where $\text{H}\alpha$ emission is strong. This may apply to the star-forming molecular cloud R3, although it also shows somewhat extended emission toward the top of the map, which the spectral index remains very flat despite no detectable $\text{H}\alpha$ emission. Another extraplanar molecular cloud, R5, exhibits visible $\text{H}\alpha$ emission with a moderately flat spectral index ($\alpha \sim -0.5$). In contrast, R6 shows a very flat spectrum despite weak $\text{H}\alpha$ emission, while R4 displays a moderately flat spectrum ($\alpha \sim -0.3$) with no indication of ongoing star formation.

5.2. Insights from Previous Simulations

While many of the flat spectra in the extraplanar clouds can be explained by enhanced thermal emission associated with star formation, some regions (R4, R6, and the region above R3) may require an alternative mechanism capable of increasing thermal emission without star formation. To gain further insight, we analyze the simulations presented in [W. Choi et al. \(2022\)](#). The simulations employ a local wind-tunnel model, in which the ICM wind is continuously driven into a local patch of the ISM disk. The ISM disk in the absence of an ICM wind is adopted from the solar-neighborhood model constructed with the TIGRESS framework ([C.-G. Kim & E. C. Ostriker 2017](#)), which self-consistently models a turbulent, magnetized ISM including radiative cooling, gaseous self-gravity, fixed stellar and dark matter gravity, and prescriptions for star formation and feedback. The simulated multiphase ISM evolves to a self-regulated, quasi-steady state, after which ICM winds of different strengths are injected from the bottom boundary of the simulation domain to model a face-on interaction. We use three models: one without an ICM wind (`noICM`) and two with weak and strong ICM winds (`ICM-P3` and `ICM-P7`, respectively). The ram pressure of the weak ICM model is comparable to the anchoring pressure ($\pi G \Sigma_{\text{gas}} \Sigma_{\text{star}}$; [J. E. Gunn & I. Gott 1972](#)), whereas that of the strong ICM model exceeds it. Full details of the simulation setup and model parameters are provided in [W. Choi et al. \(2022\)](#). Note that the ICM wind is unmagnetized.

In these simulations, ionizing radiation and CRe are not included, preventing us from producing direct synthetic observations of thermal and nonthermal emission at the radio frequencies of interest. Instead, we estimate the free-free emission using the electron density under the assumption of collisional ionization equilibrium. The volume emissivity of the free-free emission is calculated by

$$j_{\nu,ff} \propto n_e n_i T^{-0.5} e^{-h\nu/k_B T}, \quad (4)$$

which is integrated along the line-of-sight (x -axis of the simulation domain) to produce a brightness map. For the non-thermal component, we present the magnetic field strength perpendicular to the line-of-sight (i.e., $B_{\perp} = (B_y^2 + B_z^2)^{1/2}$), since the synchrotron emission strength is approximately proportional to B_{\perp} .

[Figure 10](#) shows the two-dimensional maps of the thermal emission and magnetic field for the `noICM`, `ICM-P3`, and `ICM-P7`. We select four snapshots for each model that clearly represent their distinct features. In the `noICM` model, both the free-free emission and magnetic field strength are roughly symmetric, although they undergo compression and expansion over time due to bursty star formation and feedback. In general, the vertical extent (or scale height) of the free-free emission is shorter than that of the perpendicular magnetic field strength. For example, the free-free emission decreases

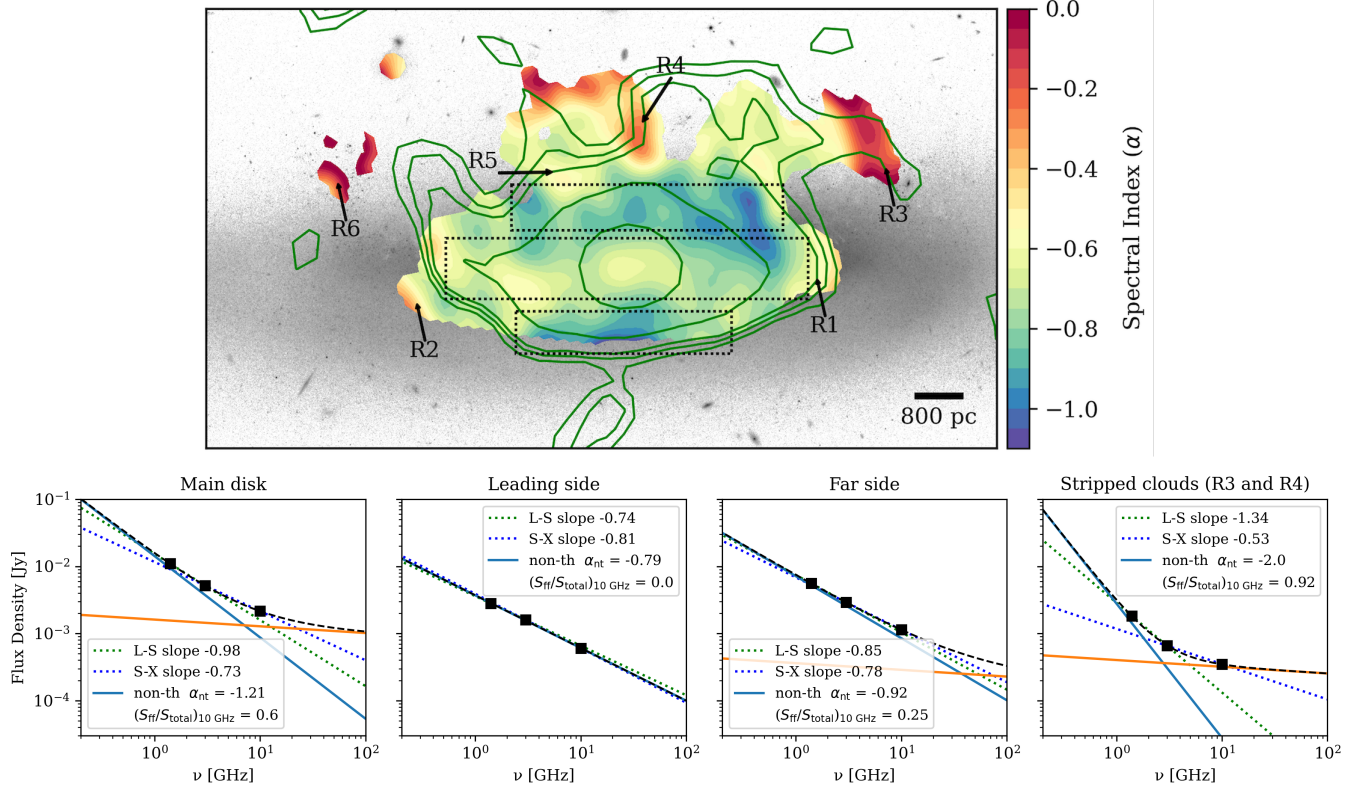


Figure 9. Top: L-band continuum intensity contours (green) overlaid on the optical and spectral index map. The contour levels of the L-band continuum emission are $(3, 4, 5, 10, 30) \times 120 \mu\text{Jy beam}^{-1}$. The black dotted boxes indicate, from bottom to top, the leading, main disk, and far side, respectively. **Bottom:** Integrated flux density spectra and two-component fits for four regions in NGC 4522. The stripped clouds corresponds to regions R3 and R4. The black squares represent the total flux densities measured in three bands (L, S, and X). The black dashed line shows the best-fit total model, composed of nonthermal (blue) and thermal (orange) components. The green and blue dotted lines indicate the spectral slopes obtained from two-band fits between the L/S and S/X bands, respectively. $(S_{\text{ff}}/S_{\text{total}})_{10 \text{ GHz}} = 0.0$ denotes the flux density ratio of the thermal to total emission at 10 GHz. All measured flux densities exceed at least four times the RMS noise level.

by a factor of 100 from the midplane to $z = 1$ kpc, whereas B_{\perp} decreases by a factor of 10. If the thermal contribution to the total emission at high frequencies (e.g., X-band) is substantial, this difference in the vertical scale heights of the two components alone can lead to a steepening of the spectral index from the midplane toward the extraplanar region. We note that the absence of ionizing radiation may reduce the overall level of free-free emission, but its scale height is expected to remain similar. The extraplanar gas density profile primarily determines the emission profile, as ionizing radiation can escape efficiently when supernovae create bubbles and fountain flows (E. Kado-Fong et al. 2020; N. B. Linzer et al. 2024).

In the ICM-P3 model, after introduction of the ICM wind, the ISM disk quickly becomes asymmetric, with gas compressed on the windward side. The compression of this leading edge of the ISM enhances the overall gas density and amplifies the magnetic field strength in the same region. At the same time, the interaction with the hot ICM, including mixing between the two media, increases the overall ISM temperature, leading to an overall enhancement of the thermal

emission compared to the noICM case. However, the extended gas on the tail side is accompanied by extended magnetic field, causing the relative contribution of the thermal and nonthermal components to remain similar. The corresponding change in the spectral index is therefore nontrivial.

Finally, the ICM-P7 model exhibits distinct behavior. The gas is gradually stripped away as the ICM ram pressure exceeds the anchoring pressure of the ISM. However, the stripping process is not impulsive. The main ISM disk is initially displaced upward by ~ 1 kpc, then falls back before being completely blown away. During this evolution, the develops an offset between the peaks of the thermal emission and magnetic field strength. This occurs primarily because the unmagnetized ICM mixes with and dilutes the magnetic field in the ISM, while the same mixing tends to maintain, or even enhance, the thermal emission, despite the absence of direct ionizing radiation. When focusing on the peak of the thermal emission (which also appears bright in other gas tracers such as H I or CO), the stripped cloud region can become almost completely dominated by thermal emission and exhibit a very flat spectral index of $\alpha \sim -0.1$.

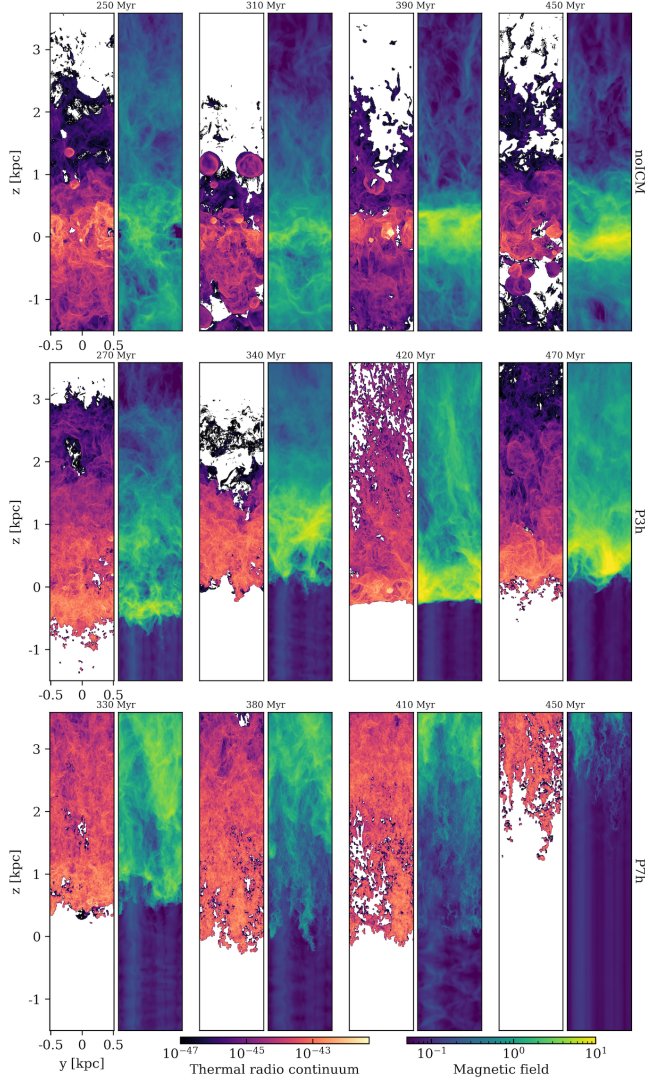


Figure 10. Two-dimensional maps of thermal emission and magnetic field strength for the noICM (top), ICM-P3 (middle), and ICM-P7 (bottom) models. The ICM wind begins to flow in at 250 Myr from the bottom boundary of the simulation box. Only the regions with $z > -1.5$ kpc is shown to focus on the upper disk. The color bars at the bottom indicated the thermal volume emissivity in $\text{erg s}^{-1} \text{cm}^{-3} \text{Hz}^{-1} \text{sr}^{-1}$ and magnetic field strength in μG .

We note that if the ICM is magnetized, a magnetic draping effect can occur, amplifying the ICM field in front of the leading side of the disk. C. Pfrommer & L. Jonathan Dursi (2010) suggested that this mechanism could explain the enhanced synchrotron emission observed on the leading side of NGC 4522, which coincides with the steepened spectral index seen in Figure 4. If this magnetic draping effect similarly influences the stripped clouds, one might expect an enhanced magnetic field near the thermal emission peak, unlike what is seen in the ICM-P7 model.

In summary, our analysis indicates that multiple mechanisms drive the observed spectral index variations: (1) a

combination of typical nonthermal emission and a moderate thermal fraction in the main disk; (2) ICM shock-induced CRe re-acceleration accompanied by suppressed thermal emission in the outer disk; and (3) strong CRe aging together with significantly enhanced thermal emission in the extraplanar clouds. For the latter, while star formation contributes where present, we propose that thermal enhancement through ICM-ISM mixing may play a critical role in regions lacking active star formation.

5.3. Comparison with ionized gas properties from MAUVE-MUSE

In this section, we compare our radio continuum results with recent MUSE observations of NGC 4522, obtained as part of the Multiphase Astrophysics to Unveil the Virgo Environment (MAUVE) project (A. B. Watts et al. 2024; B. Catinella et al. 2025). In particular, T. Brown et al. (2025) conducted a detailed analysis of the ionization sources in Virgo galaxies, highlighting the diverse processes influencing the warm phase of the ISM. Here, we use the same MUSE dataset for NGC 4522, with the only difference being that our line maps are generated without pre-masking and by binning the data cube to achieve a SNR of 10 in the 6760 – 6790 Å wavelength range (corresponding to the [S II] doublet), in order to maximize sensitivity to diffuse extraplanar emission. This differs from the approach adopted by Brown et al., who used a SNR threshold based on the 4800 – 7000 Å range and pre-masked individual spaxels with $\text{S/N} < 1.5$.

Figure 11 shows the two-dimensional distribution of the $[\text{S II}] \lambda 6716, 6731/\text{H}\alpha$ (the corresponding $[\text{N II}] \lambda 6583/\text{H}\alpha$ map is shown in Figure 15). We include only spaxels with S/N greater than 3 and flux densities higher than $1 \times 10^{-19} \text{ erg cm}^{-2} \text{s}^{-1}$. We are unable to correct these ratios for dust attenuation because of the low S/N of the $\text{H}\beta$ line in the extraplanar region. However, dust has only a minor effect on the $[\text{S II}]/\text{H}\alpha$ ratio and a negligible effect on the $[\text{N II}]/\text{H}\alpha$ (D. E. Osterbrock & G. J. Ferland 2006). These maps reveal that most of the main disk is characterized by line ratios consistent with ionization by star formation (i.e., low $[\text{S II}]/\text{H}\alpha$ and $[\text{N II}]/\text{H}\alpha$), whereas several regions in the outer disk and extraplanar area exhibit elevated $[\text{S II}]/\text{H}\alpha$ ratios, likely tracing ICM interaction and shock excitation in NGC 4522.

First, they identify prominent shock-induced features (very high $[\text{S II}]/\text{H}\alpha$) in the outer disk (i.e., the leading and far sides), where steep spectral indices ($\alpha < -0.7$) are observed in Figure 4. This is expected, as shocked gas emits a synchrotron-dominated continuum due to CRe re-acceleration. This interpretation is also supported by the two-component analysis in this region (Figure 9), which reveals a nearly pure power-law spectrum without the curvature characteristic of radiative cooling. Moreover, the nonthermal spectral index (α_{nt}) in these regions is found to be flatter than

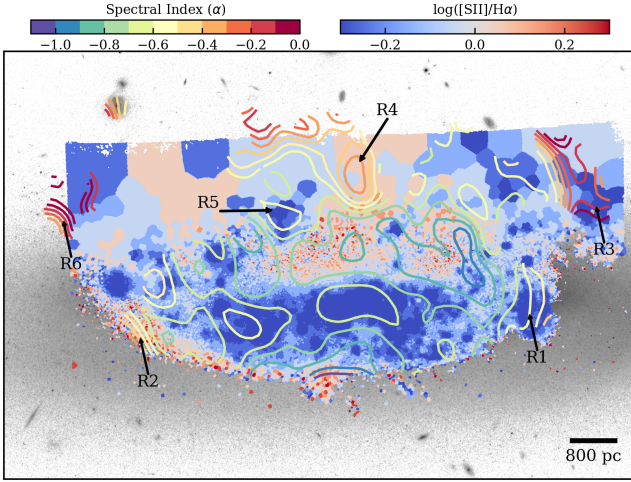


Figure 11. Map of [S II]/H α from MUSE observations (MAUVE-MUSE; T. Brown et al. 2025), overlaid with the contours of the spectral index between S and X bands.

that of the main disk. The coincidence of these spectral features and high [S II]/H α ratios provides a coherent picture, confirming that the ICM shock likely governs the emission properties on both the leading and far sides of the outer disk.

In the main disk, both [S II]/H α and [N II]/H α are low, clearly indicating that star formation is the dominant source of ionization. This is consistent with the relatively flat spectral index (-0.6) observed in this region. Although R5 is located in the extraplanar region, its behavior is similar to that of the main disk, showing low [S II]/H α and [N II]/H α ratios and a relatively flat spectral index. Intriguingly, the vicinity of R5 exhibits similarly flat spectral indices despite the absence of detectable H α emission. This suggests that the ICM-ISM mixing affects the extraplanar gas, or that effective diffusion of free electrons enhances the thermal emission without triggering star formation, therefore without producing detectable H α emission.

Other regions, however, exhibit more complex features. R3 shows clear H α emission with a low [S II]/H α ratio, and R4 exhibits a high [S II]/H α ratio but no detectable H α emission. Despite these differences in ionized gas properties, both regions display a very flat spectral index ($\alpha > -0.3$). R2 shows a high [S II]/H α ratio without strong H α emission, similar to the leading side of the galaxy. However, its spectral index is much flatter than that of the leading side, suggesting that both the ICM shock and ICM-ISM mixing influence R2. In contrast, R1 exhibits strong H α emission with low [S II]/H α and [N II]/H α ratios, indicating that it is primarily affected by star formation. Nevertheless, we speculate that R1 may also experience some influence from the ICM-ISM mixing, as its spectral index tentatively flattens outward in a manner similar to R2.

Consequently, we can classify NGC 4522 into four categories: (1) Strong SF and synchrotron emission (main disk), (2) Strong SF with mixing and synchrotron emission (R1 and R5), (3) Weak or no SF with mixing and shock-induced synchrotron emission (outer disk and R2), and (4) Mixing and CRe aging (R3, R4, and R6). The characteristics of each region are summarized in Table 3. To facilitate the interpretation of these properties, Figure 12 shows a schematic overview and a profile view of NGC 4522, illustrating the geometry and spatial distribution of different emission components relative to the ICM wind.

5.4. Highly Asymmetric Polarized Emissions

We detected highly asymmetric polarized emission in both S- and X-bands, as described in Section 4. Such features are rarely observed in nearby field galaxies, even among highly inclined galaxies (e.g., R. Beck 2005; M. Krause et al. 2020), whereas 16 out of 29 observed Virgo spiral galaxies exhibit strongly asymmetric polarized emission (B. Vollmer et al. 2004, 2007, 2013). This suggests that the observed asymmetry is not solely due to the viewing-angle effect but is instead driven by environmental influences within the galaxy cluster, including ram pressure by the ICM. Compression and shear motions, caused by ram pressure, tidal interactions, gas accretion, or magnetic draping, have been proposed as the most likely mechanisms responsible for the enhanced polarized emission on the leading sides of galaxies (e.g., B. Vollmer et al. 2006; C. Pfrommer & L. Jonathan Dursi 2010). While these mechanisms can explain the aligned magnetic field and enhanced polarization on the leading side, they do not account for the absence of polarized emission in the remaining regions of our target, which ultimately results in the strongly asymmetric morphology.

We conjecture that the highly asymmetric polarized emission arises from a combination of enhanced polarization on the leading side and reduced polarized emission across the main disk. The ICM wind sweeping across the disk can disrupt the regular magnetic field while simultaneously enhancing (or maintaining) the turbulent magnetic component in the same region. This process likely decreases the polarized emission within the disk, even though the total continuum emission remains largely unchanged. To test this hypothesis, we estimate the evolution of the regular and turbulent magnetic fields using the simulations described in Section 5.1. We calculate regular and turbulent magnetic fields as $B_{\text{reg}} = (\bar{B}_x^2 + \bar{B}_y^2 + \bar{B}_z^2)^{0.5}$ and $B_{\text{turb}} = ((B_x - \bar{B}_x)^2 + (B_y - \bar{B}_y)^2 + (B_z - \bar{B}_z)^2)^{0.5}$, respectively, where $B_{x,y,z}$ are the magnetic field components in each simulation cell along the x , y , z directions, and the mean magnetic field, $\bar{B}_{x,y,z}$, are their mean values, computed by averaging each component over the horizontal ($x - y$) plane at a given vertical height z . To quantify the ratio between the

Location	Spectral Index	H α	log([S II]/H α)	Thermal	Nonthermal
Main disk	$-0.8 \lesssim \alpha \lesssim -0.5$	Strong	-0.6 – -0.2	SF	Sync
Leading side	$-1.1 \lesssim \alpha \lesssim -0.7$	Weak	0 – 0.4	–	Shock + Sync
Far side	$-1.1 \lesssim \alpha \lesssim -0.6$	Weak	0 – 0.4	–	Shock + Sync
R1	-0.61 ± 0.22	Strong	-0.4 – 0	SF + Mixing?	Sync
R2	-0.56 ± 0.25	Weak	0.1 – 0.4	Mixing	Sync + Shock?
R3	-0.16 ± 0.21	Moderate	-0.2 – 0	SF + Mixing	CRe aging
R4	-0.36 ± 0.05	Weak	-0.1 – 0.1	Mixing	CRe aging
R5	-0.63 ± 0.11	Moderate	-0.3 – 0	SF + Mixing	Sync + Shock?
R6	-0.13 ± 0.08	None	None	Mixing	CRe aging

Table 3. Summary of regional characteristics. The spectral indices and log([S II/H α]) for the main disk, leading side, and far side are measured across each respective region, whereas those for R1 – R6 are measured within a region corresponding to two synthesized beam sizes.

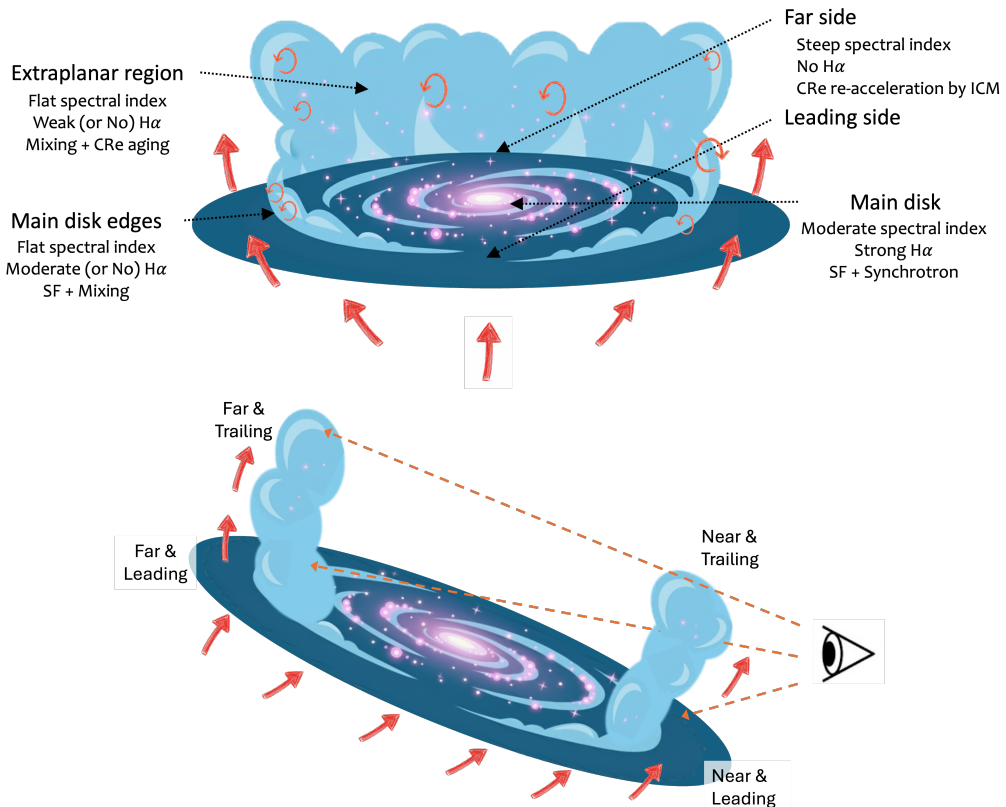


Figure 12. Schematic overview and geometry of NGC 4522. The red arrows show the ICM wind direction. **Top:** A face-on view highlighting regions of interest (the main disk, the outer disk, and the extraplanar regions) and their characteristics. **Bottom:** A profile view illustrating the relative geometry between the observer and the galaxy. The diagram defines the far/near and leading/trailing sides and show the potential line-of-sight confusion between different regions. Note that, for visual clarity, stripped gas components in the central part of the diagrams are omitted in both panels.

regular and turbulent fields ($B_{\text{reg}}/B_{\text{turb}}$) within the disk, we consider the region within ± 300 pc of the midplane. In the noICM model, this ratio ranges between 0.2 and 0.8 (mean ≈ 0.5) over 250 Myr, with $B_{\text{reg}} = 0.3 - 3.5 \mu\text{G}$ and $B_{\text{turb}} = 1 - 5 \mu\text{G}$. In the ICM-P3 model, the ratio decreases to 0.1 – 0.4 (mean ≈ 0.3) over the same period, with $B_{\text{reg}} = 0.2 - 2.5 \mu\text{G}$ and $B_{\text{turb}} = 1 - 6.5 \mu\text{G}$. These results indicate that

ram pressure can suppress the regular magnetic field while enhancing the turbulent component, thereby reducing the polarized emission from the disk.

In addition to the increased turbulent-to-regular magnetic field ratio, Faraday depolarization is also likely to contribute to the suppression of polarized emission. T. G. Arshakian & R. Beck (2011) demonstrated that the intensity of polarized

radio continuum emission decreases as a function of the rotation measure (RM) at a given wavelength. Since the RM is proportional to both the electron density and the line-of-sight magnetic field component (Equation 2), enhancements in either quantity will increase the RM and, consequently, reduce the polarized emission. Although we could not directly measure the magnetic field strength in the regions lacking polarized emission, the regions where polarization is detected exhibit relatively weak magnetic fields. This suggests that an increase in electron density is the more plausible cause of the depolarization. This interpretation is consistent with our earlier suggestion that ICM–ISM mixing, which can heat the ISM and produce additional free electrons, plays an important role in shaping the overall ISM properties of NGC 4522.

Consequently, the combination of these suppression effects with mechanisms that enhance polarized emission on the leading side, such as compression, shear motions, and magnetic draping, can naturally explain the highly asymmetric polarized emission observed in NGC 4522.

6. SUMMARY

We present S-band (3 GHz) and X-band (10 GHz) VLA continuum observations of the ram pressure–stripped galaxy NGC 4522 at spatial resolutions of $\sim 7''$ and $\sim 2.5''$, respectively. The VLA data were calibrated to obtain both total and polarized radio continuum maps. We examine the overall distribution of the total continuum in comparison with multi-wavelength observations and analyze the spectral index distribution and investigate the physical mechanisms driving its variation. Using the polarized continuum data, we investigate the spatial distribution of polarized emission, magnetic field orientations, and polarization fraction variations, and discuss the physical origins of the highly asymmetric polarized morphology. We further derive the rotation measure from the polarization angles in both bands, estimate magnetic field strengths, and discuss their implications.

The main findings are summarized as follows:

1. The total radio continuum emission at S and X bands is asymmetric, extending toward the northwest, broadly resembling the H I gas distribution. Within the stellar disk, continuum emissions spatially correlate with CO and $H\alpha$, whereas the extraplanar regions exhibit local offsets, suggesting a complex interplay between the ISM and the ICM. The integrated spectral index between the S and X bands ($\alpha = -0.93 \pm 0.05$) is consistent with previous L- and C-band measurements ($\alpha = -0.97$, [B. Vollmer et al. 2004](#)). However, our 2D spectral index map (Figure 4) reveals, for the first time, significantly flatter indices in the extraplanar regions.
2. The spectral index steepens systematically from $\alpha \sim -0.6$ in the main disk to $\alpha \sim -1.1$ in the outer disk. The galaxy's leading side, directly impacted by the ICM wind, shows moderately steep indices ($\alpha \approx -0.8$), and the far side also shows similar spectral slopes. Two component fitting shows that the outer disk exhibits a near pure power-law spectrum without clear evidence of CRe aging and their non-thermal spectral index is flatter compared to the main disk. These features suggest recent CRe re-acceleration by the ICM-induced shock. A significant reduction in the contribution from thermal emission is observed across the outer disk.
3. Extraplanar clouds (R3 – R6) exhibit unusually flat spectral indices ($\alpha \sim -0.3$ to 0). While some regions coincide with strong $H\alpha$ emission (e.g., R3 and R5), others show little or no detectable $H\alpha$ (e.g., R4, R6). These flat indices result from a combination of strongly aged, steep nonthermal spectra and significantly enhanced thermal emission. We propose that ICM–ISM mixing serves as the primary mechanism enhancing thermal emission independent of star formation. Our previous simulations support this scenario, demonstrating that stripped clouds mixed with the ICM can sustain thermal emission while the magnetic field becomes diluted. The mild flattening observed at the edges of the main disk (R1 with $H\alpha$ and R2 without $H\alpha$) may also partly arise from such mixing processes.
4. Polarized continuum emission in both bands is highly asymmetric, although spatial offsets exist between the locations and distributions of their peaks. The magnetic field orientation in the X-band is nearly parallel to the galactic disk, whereas in the S-band it tends to be rotated toward the north. In both bands, the polarization fraction increases radially outward from the galaxy center, suggesting that the polarized continuum emission may originate from gas compression by the ICM wind and/or the magnetic draping effect. The overall polarization fraction is higher in the X-band, likely because the S-band is more strongly affected by Faraday depolarization.
5. Using polarization angles from both bands, we derive rotation measures (RM) and estimate the line-of-sight magnetic field strength. Due to the limited wavelength coverage, we adopt a foreground screen model rather than performing RM synthesis analysis. The RMs range from -100 to 350 rad m^{-2} , clustering around two main intervals: -100 to 0 and 200 to 300 rad m^{-2} . The estimated line-of-sight magnetic field strengths range from 0 to $15 \mu\text{G}$, with a median value of $\approx 6 \mu\text{G}$, while those within the main disk remain relatively low ($\lesssim 5 \mu\text{G}$).

6. We suggest that the highly asymmetric polarized emission arises from a combination of two effects: enhanced polarized emission at the leading side, likely due to the compression and the magnetic draping via RPS; and suppressed polarized emission within the disk, where the interaction with the ICM increases turbulent magnetic fields and CR electrons, while regular magnetic fields are reduced by ICM shock propagation.

Although we showed Appendix B that convolving the X-band images has only a minor impact on the overall results, it would be preferable to obtain images with similar spatial resolution to minimize uncertainties introduced during post-processing. Therefore, we plan to propose additional VLA observations of NGC 4522 at lower-resolution X-band (or high-resolution S-band) to improved both the image consistency and sensitivity. Moreover, since our current analysis is based on a single galaxy, we will also propose VLA observations of other Virgo galaxies exhibiting clear extraplanar gas to test our hypothesis. These future observations will help determine whether NGC 4522 represents a unique case and provide a deeper understanding of ram-pressure effects on the general ISM. Finally, while our simulation analysis has provided valuable insights, quantitative interpretation was limited by the absence of CRe and the restricted simulation volume. A galaxy-scale simulation incorporating both magnetic fields and CRe would enable a more complete investigation of the evolution of thermal and nonthermal radio emission.

ACKNOWLEDGMENTS

We thank the anonymous referee for helpful and constructive comments. The work of WC was supported by Basic Science Research Program through the National Research Foundation of Korea (NRF) funded by the Ministry of Education (RS-2024-00413394). AC acknowledges support by the NRF, No. RS-2022-NR070872 and RS-2022-NR069020.

This work has used the Karl G. Jansky Very Large Array operated by the National Radio Astronomy Observatory (NRAO). The NRAO and Green Bank Observatory are facilities of the U.S. National Science Foundation operated under cooperative agreement by Associated Universities, Inc. All the *HST* data presented in this paper were obtained from the Mikulski Archive for Space Telescopes (MAST) at the Space Telescope Science Institute. The specific observations analyzed can be accessed via MAST: [10.17909/pahn-3r19](https://doi.org/10.17909/pahn-3r19). STScI is operated by the Association of Universities for Research in Astronomy, Inc., under NASA contract NAS5-26555. Support to MAST for these data is provided by the NASA Office of Space Science via grant NAG5-7584 and by other grants and contracts.

Facilities: VLA

Software: astropy (Astropy Collaboration et al. 2013, 2018), matplotlib (J. D. Hunter 2007), numpy (C. R. Harris et al. 2020), scipy (P. Virtanen et al. 2020) APLpy (T. Robitaille & E. Bressert 2012)

APPENDIX

A. DATA REDUCTION

The data were reduced using the COMMON ASTRONOMY SOFTWARE APPLICATIONS (CASA; J. P. McMullin et al. 2007), version 6.4.1. Each observation was processed in an identical manner. To obtain the polarization information from the VLA continuum observations, we calibrated the data as follows¹¹:

1. Run the pipeline, which is provided by the NRAO, using CASA. By doing so, we obtained the calibrated parallel-hand (RR/LL)¹² cross-correlation visibilities, which allow us to derive only the total intensity of the continuum rather than the polarization information. Therefore, additional calibration steps were required to obtain the polarized continuum.
2. To continue the polarization calibration, we needed to remove the parallactic-angle correction that had been applied by the standard pipeline. Therefore, we ran the task `applycal`, reapplying the calibration to the corrected column with `parang=False`, thereby disabling the parallactic-angle corrections. Subsequently, the parallel-hand (RR and LL) data for all calibrators and for the target were flagged to remove severe radio-frequency interference (RFI) using the task `flagdata` with the mode set to "rflag".
3. Another round of RFI flagging was performed for the parallel-hand data of all calibrators using the mode 'tfcrop', and for the cross-hand data (RL and LR) of all calibrators using the mode "rflag", with the `flagdata` task. In addition, manual flagging was carried out on the calibrators to remove low-level RFI and bad data that were not eliminated during the previous

¹¹ Note that these reductions are consistent with the standard continuum reduction tutorials (see https://casaguides.nrao.edu/index.php?title=CASA_Guides:Polarization_Calibration_based_on_CASA_pipeline_standard_reduction:_The_radio_galaxy_3C75-CASA6.4.1). The parameters and options were adjusted to reflect the characteristics of our observations.

¹² Note that the VLA antennas detect right- (R) and left-hand (L) circularly polarized emission.

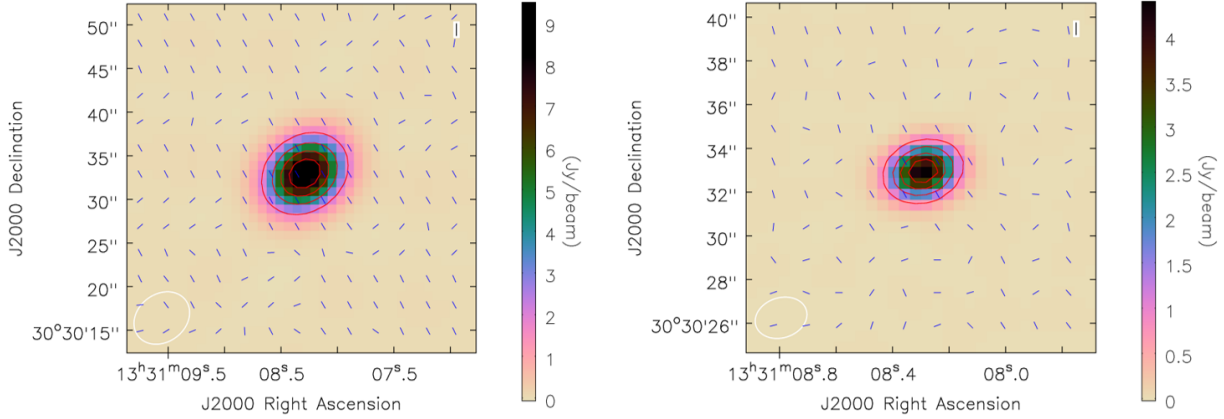


Figure 13. Total continuum intensity maps of 3C 286 overlaid with the polarized intensity (red contours) and polarization angle (blue vectors) for the S-band (left) and X-band (right). Contour levels are $(0.2, 0.4, 0.6, 0.8) \times 1.02$ (0.53) Jy beam $^{-1}$ for the S-band (X-band). The synthesized beams of $7''.9 \times 6''.0$ and $2''.2 \times 1''.9$, respectively, and are shown in the bottom-left corner of the maps. These results confirm the accuracy of our data calibration.

flagging steps. During this process, spectral window 3 (spw3) was completely flagged for both the parallel- and cross-hand data of all calibrators and the target source due to severe RFI contamination.

4. We set the full polarization models for the flux-density, phase, and polarization-leakage calibrators using the polarization fractions and position angles as functions of frequency derived by [R. A. Perley & B. J. Butler \(2017\)](#). These models were then used as reference values for the subsequent calibration steps.
5. To determine the instrumental delay between the two polarization outputs, we derived the cross-hand delay ("kcross") solutions using a calibrator with known polarization. For this purpose, 3C 286 was used to solve for the cross-hand delays with the task `gaintcal`.
6. To determine the frequency-dependent polarization leakage between the R and L polarization channels (the so-called D-terms), which arise from instrumental effects, we solved for the polarization leakage per channel using the unpolarized calibrator J1407+2827 with the task `polcal` and `poltype="Df"`.
7. To determine the absolute polarization angle (Xf), we ran the task `polcal` with `poltype="Xf"`, using a calibrator with a known polarization position angle (3C 286).
8. We then applied all calibration solutions to the raw data, including all three calibrators and the target source (NGC 4522), using the `applycal` task with `parang=True`.

To assess the robustness of our calibration, we first imaged the well-known calibrator 3C 286 and measured its total continuum flux, polarized flux, and polarization angle. The same imaging parameters and pixel scales as described above were used. [Figure 13](#) presents the total-intensity maps overlaid with the polarized continuum (red contours) and polarization angles (blue vectors) for the S-band (left) and X-band (right) of 3C 286. The measured total flux densities of 3C 286 are 10.0 Jy at S-band and 4.6 Jy at X-band; the polarized flux densities are 1.07 Jy and 0.55 Jy, respectively; and the polarization angles are 33.4° and 33.9° , respectively. The corresponding reference values reported by ([R. A. Perley & B. J. Butler 2017](#)) are 9.92 Jy at 3 GHz and 4.53 Jy at 10 GHz, 1.09 Jy at 3 GHz and 0.55 Jy at 10 GHz, and 33.0° at 3 GHz and 33.4° at 10 GHz, respectively. These results confirm that our polarization calibration was performed successfully.

To produce a clean image of our target, we first generated a mask interactively using the `tclean` task, defining the regions where the algorithm was allowed to search for emission and encompassing all bright sources. We then deconvolved the calibrated data with `tclean` using the generated mask, cleaning down to a threshold of twice the RMS noise of the dirty image. The cleaned components were imaged with Briggs weighting, adopting a robust parameter of 0.5 for the S band and 1.5 for the X band. During imaging, we employed the *Multi-scale Multi-frequency* (MT-MFS, [U. Rau & T. J. Cornwell 2011](#)) algorithm, which improves upon the traditional CLEAN method for wide-band VLA observations. In this scheme, `tclean` was set to converge at spatial scales corresponding to the synthesized beam, 5 \times the synthesized beam, and 15 \times the synthesized beam. Compared

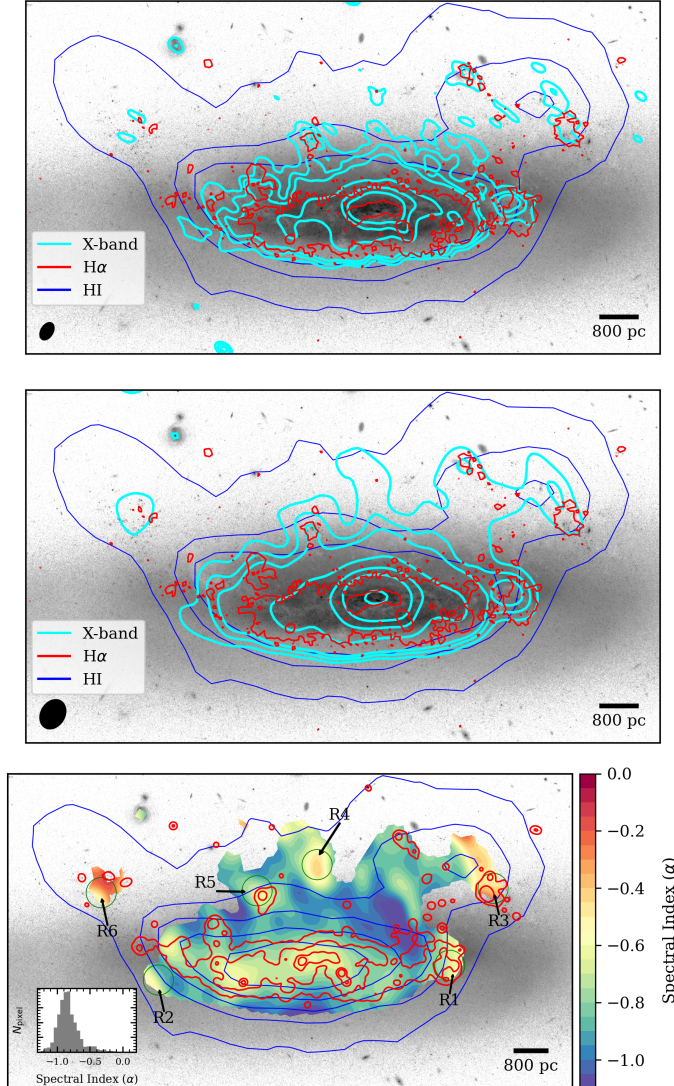


Figure 14. Same as Figure 2, but for the UV-tapered X-band continuum map (top) and the X-band map convolved to the S-band resolution (middle). The UV range above $30k\lambda_{3\text{cm}}$ was tapered, resulting in a synthesized beam of $4''.7 \times 3''.0$. The bottom panel shows the spectral index map derived from the UV-tapered X-band and S-band maps.

with traditional CLEAN algorithms, MT-MFS models source structures as a collection of truncated paraboloids rather than point sources and simultaneously accounts for spectral variations of the source flux across the observing bandwidth. These features make MT-MFS particularly well suited for our data, as NGC 4522 exhibits extended radio continuum emission and the VLA observations cover a wide frequency range.

Consequently, we achieved synthesized beam sizes of $7''.9 \times 6''.0$ for the S-band and $2''.6 \times 2''.1$ for the X-band in the final images of NGC 4522. To balance spatial sampling against image size, pixel sizes of 1.2 arcsec and 0.5 arcsec were adopted for the S- and X-bands, respectively, corresponding to ≈ 5.8 and ≈ 4.7 pixels across the synthesized beams.

We did not apply any correction for Faraday rotation, as we intended to present the observed polarization angles directly. The rotation measure (RM) ranges from -100 to 300 rad m^{-1} , corresponding to a Faraday rotation of approximately -57 to 180 deg in the S band (see Section 4.3). Because Faraday rotation scales as λ^2 , its effect at X-band (3 cm) is expected to be negligible. In addition, the Galactic rotation measure toward NGC 4522 is less than 20 rad m^{-2} (A. R. Taylor et al. 2009), and thus no correction for the Milky Way contribution was applied.

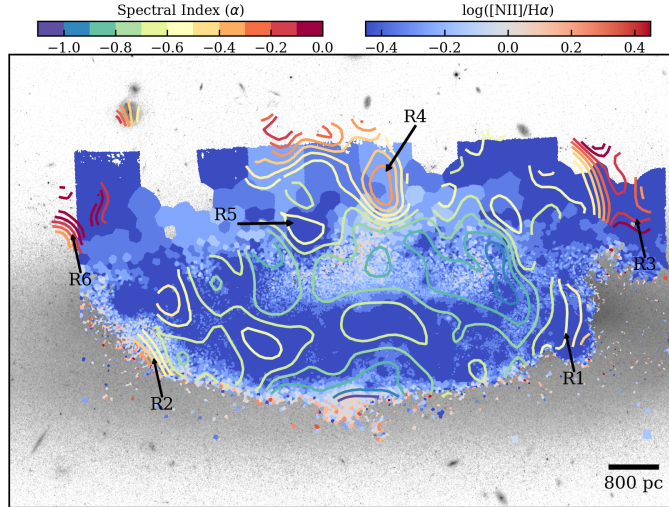


Figure 15. A map [N II]/H α from MUSE observations, overlaid with contours of the spectral index map.

B. TEST OF X-BAND IMAGING AND SMOOTHING

In Figure 14, we present the UV-tapered X-band continuum map (top) and the X-band map convolved to the S-band resolution (middle). The UV range above $30\text{k}\lambda_{\text{3cm}}$, resulting in a synthesized beam of $4''.7 \times 3''.0$ and an RMS noise of $2 \mu\text{Jy beam}^{-1}$. The bottom panel shows the spectral index map derived from the UV-tapered X-band and S-band maps. The overall trend of the spectral index is similar to that in Figure 4, although the values are systematically lower by approximately 0.15.

C. [N II]/H α MAP

Figure 15 is the same as Figure 11, but for [N II]/H α . Although the overall values are lower than those of [S II]/H α , the general trend remains very similar.

REFERENCES

Abramson, A., Kenney, J., Crowl, H., & Tal, T. 2016, AJ, 152, 32, doi: [10.3847/0004-6256/152/2/32](https://doi.org/10.3847/0004-6256/152/2/32)

Abramson, A., & Kenney, J. D. P. 2014, AJ, 147, 63, doi: [10.1088/0004-6256/147/3/63](https://doi.org/10.1088/0004-6256/147/3/63)

Abramson, A., Kenney, J. D. P., Crowl, H. H., et al. 2011, AJ, 141, 164, doi: [10.1088/0004-6256/141/5/164](https://doi.org/10.1088/0004-6256/141/5/164)

Arshakian, T. G., & Beck, R. 2011, MNRAS, 418, 2336, doi: [10.1111/j.1365-2966.2011.19623.x](https://doi.org/10.1111/j.1365-2966.2011.19623.x)

Astropy Collaboration, Robitaille, T. P., Tollerud, E. J., et al. 2013, A&A, 558, A33, doi: [10.1051/0004-6361/201322068](https://doi.org/10.1051/0004-6361/201322068)

Astropy Collaboration, Price-Whelan, A. M., Sipőcz, B. M., et al. 2018, AJ, 156, 123, doi: [10.3847/1538-3881/aabc4f](https://doi.org/10.3847/1538-3881/aabc4f)

Beck, R. 2001, SSRv, 99, 243, <https://arxiv.org/abs/astro-ph/0012402>

Beck, R. 2005, in Cosmic Magnetic Fields, ed. R. Wielebinski & R. Beck, Vol. 664, 41, doi: [10.1007/3540313966_3](https://doi.org/10.1007/3540313966_3)

Beck, R. 2015, A&A Rv, 24, 4, doi: [10.1007/s00159-015-0084-4](https://doi.org/10.1007/s00159-015-0084-4)

Boselli, A., Fossati, M., Ferrarese, L., et al. 2018, A&A, 614, A56, doi: [10.1051/0004-6361/201732407](https://doi.org/10.1051/0004-6361/201732407)

Brentjens, M. A., & de Bruyn, A. G. 2005, A&A, 441, 1217, doi: [10.1051/0004-6361:20052990](https://doi.org/10.1051/0004-6361:20052990)

Brown, T., Brown, T., Brown, T., et al. 2025 ApJ, submitted

Catinella, B., Cortese, L., Sun, J., et al. 2025, The Messenger, 195, 15, doi: [10.18727/0722-6691/5393](https://doi.org/10.18727/0722-6691/5393)

Cayatte, V., van Gorkom, J. H., Balkowski, C., & Kotanyi, C. 1990, AJ, 100, 604, doi: [10.1086/115545](https://doi.org/10.1086/115545)

Choi, W., Kim, C.-G., & Chung, A. 2022, ApJ, 936, 133, doi: [10.3847/1538-4357/ac82ba](https://doi.org/10.3847/1538-4357/ac82ba)

Chung, A., van Gorkom, J. H., Kenney, J. D. P., Crowl, H., & Vollmer, B. 2009, AJ, 138, 1741, doi: [10.1088/0004-6256/138/6/1741](https://doi.org/10.1088/0004-6256/138/6/1741)

Chyží, K. T., Ehle, M., & Beck, R. 2007, A&A, 474, 415, doi: [10.1051/0004-6361:20077497](https://doi.org/10.1051/0004-6361:20077497)

Condon, J. J. 1992, ARA&A, 30, 575, doi: [10.1146/annurev.aa.30.090192.003043](https://doi.org/10.1146/annurev.aa.30.090192.003043)

Condon, J. J., Cotton, W. D., Greisen, E. W., et al. 1998, AJ, 115, 1693, doi: [10.1086/300337](https://doi.org/10.1086/300337)

Cortese, L., Ciesla, L., Boselli, A., et al. 2012, A&A, 540, A52, doi: [10.1051/0004-6361/201118499](https://doi.org/10.1051/0004-6361/201118499)

Crowl, H. H., & Kenney, J. D. P. 2006, ApJL, 649, L75, doi: [10.1086/508344](https://doi.org/10.1086/508344)

Crowl, H. H., & Kenney, J. D. P. 2008, AJ, 136, 1623, doi: [10.1088/0004-6256/136/4/1623](https://doi.org/10.1088/0004-6256/136/4/1623)

Crowl, H. H., Kenney, J. D. P., van Gorkom, J. H., & Vollmer, B. 2005, AJ, 130, 65, doi: [10.1086/430526](https://doi.org/10.1086/430526)

Dressler, A. 1980, ApJ, 236, 351, doi: [10.1086/157753](https://doi.org/10.1086/157753)

Gioia, I. M., Gregorini, L., & Klein, U. 1982, A&A, 116, 164

Gunn, J. E., & Gott, J. Richard, I. 1972, ApJ, 176, 1, doi: [10.1086/151605](https://doi.org/10.1086/151605)

Harris, C. R., Millman, K. J., van der Walt, S. J., et al. 2020, Nature, 585, 357, doi: [10.1038/s41586-020-2649-2](https://doi.org/10.1038/s41586-020-2649-2)

Heesen, V., Whitler, L., Schmidt, P., et al. 2019, A&A, 628, L3, doi: [10.1051/0004-6361/201936046](https://doi.org/10.1051/0004-6361/201936046)

Hummel, E., Dahlem, M., van der Hulst, J. M., & Sukumar, S. 1991, A&A, 246, 10

Hunter, J. D. 2007, Computing in Science and Engineering, 9, 90, doi: [10.1109/MCSE.2007.55](https://doi.org/10.1109/MCSE.2007.55)

Ignesti, A., Vulcani, B., Botteon, A., et al. 2023, A&A, 675, A118, doi: [10.1051/0004-6361/202346517](https://doi.org/10.1051/0004-6361/202346517)

Kado-Fong, E., Kim, J.-G., Ostriker, E. C., & Kim, C.-G. 2020, ApJ, 897, 143, doi: [10.3847/1538-4357/ab9abd](https://doi.org/10.3847/1538-4357/ab9abd)

Kenney, J. D. P., Geha, M., Jächym, P., et al. 2014, ApJ, 780, 119, doi: [10.1088/0004-637X/780/2/119](https://doi.org/10.1088/0004-637X/780/2/119)

Kenney, J. D. P., van Gorkom, J. H., & Vollmer, B. 2004, AJ, 127, 3361, doi: [10.1086/420805](https://doi.org/10.1086/420805)

Kim, C.-G., & Ostriker, E. C. 2017, ApJ, 846, 133, doi: [10.3847/1538-4357/aa8599](https://doi.org/10.3847/1538-4357/aa8599)

Klein, U., & Fletcher, A. 2015, Galactic and Intergalactic Magnetic Fields

Klein, U., Wielebinski, R., & Beck, R. 1984, A&A, 133, 19

Koopmann, R. A., & Kenney, J. D. P. 2004, ApJ, 613, 851, doi: [10.1086/423190](https://doi.org/10.1086/423190)

Krause, M., Irwin, J., Schmidt, P., et al. 2020, A&A, 639, A112, doi: [10.1051/0004-6361/202037780](https://doi.org/10.1051/0004-6361/202037780)

Lee, B., & Chung, A. 2018, ApJ, 866, L10, doi: [10.3847/2041-8213/aae4d9](https://doi.org/10.3847/2041-8213/aae4d9)

Linzer, N. B., Kim, J.-G., Kim, C.-G., & Ostriker, E. C. 2024, ApJ, 975, 173, doi: [10.3847/1538-4357/ad7733](https://doi.org/10.3847/1538-4357/ad7733)

Longair, M. S. 2011, High Energy Astrophysics

Makarov, D., Prugniel, P., Terekhova, N., Courtois, H., & Vauglin, I. 2014, A&A, 570, A13, doi: [10.1051/0004-6361/201423496](https://doi.org/10.1051/0004-6361/201423496)

McMullin, J. P., Waters, B., Schiebel, D., Young, W., & Golap, K. 2007, in Astronomical Society of the Pacific Conference Series, Vol. 376, Astronomical Data Analysis Software and Systems XVI, ed. R. A. Shaw, F. Hill, & D. J. Bell, 127

Orlando, E. 2018, MNRAS, 475, 2724, doi: [10.1093/mnras/stx3280](https://doi.org/10.1093/mnras/stx3280)

Osterbrock, D. E., & Ferland, G. J. 2006, Astrophysics of gaseous nebulae and active galactic nuclei

Padovani, M., Bracco, A., Jelić, V., Galli, D., & Bellomi, E. 2021, A&A, 651, A116, doi: [10.1051/0004-6361/202140799](https://doi.org/10.1051/0004-6361/202140799)

Padovani, M., Ivlev, A. V., Galli, D., & Caselli, P. 2018, A&A, 614, A111, doi: [10.1051/0004-6361/201732202](https://doi.org/10.1051/0004-6361/201732202)

Perley, R. A., & Butler, B. J. 2017, ApJS, 230, 7, doi: [10.3847/1538-4365/aa6df9](https://doi.org/10.3847/1538-4365/aa6df9)

Pfrommer, C., & Jonathan Dursi, L. 2010, Nature Physics, 6, 520, doi: [10.1038/nphys1657](https://doi.org/10.1038/nphys1657)

Ramatsoku, M., Serra, P., Poggianti, B. M., et al. 2019, MNRAS, 487, 4580, doi: [10.1093/mnras/stz1609](https://doi.org/10.1093/mnras/stz1609)

Rau, U., & Cornwell, T. J. 2011, A&A, 532, A71, doi: [10.1051/0004-6361/201117104](https://doi.org/10.1051/0004-6361/201117104)

Roberts, I. D., van Weeren, R. J., Timmerman, R., et al. 2022, A&A, 658, A44, doi: [10.1051/0004-6361/202142294](https://doi.org/10.1051/0004-6361/202142294)

Roberts, I. D., van Weeren, R. J., McGee, S. L., et al. 2021, A&A, 650, A111, doi: [10.1051/0004-6361/202140784](https://doi.org/10.1051/0004-6361/202140784)

Roberts, I. D., van Weeren, R. J., Lal, D. V., et al. 2024, A&A, 683, A11, doi: [10.1051/0004-6361/202347977](https://doi.org/10.1051/0004-6361/202347977)

Robitaille, T., & Bressert, E. 2012, APLpy: Astronomical Plotting Library in Python, Astrophysics Source Code Library, record ascl:1208.017 <http://ascl.net/1208.017>

Stein, M., Heesen, V., Dettmar, R. J., et al. 2023, A&A, 670, A158, doi: [10.1051/0004-6361/202243906](https://doi.org/10.1051/0004-6361/202243906)

Tabatabaei, F. S., Schinnerer, E., Krause, M., et al. 2017, ApJ, 836, 185, doi: [10.3847/1538-4357/836/2/185](https://doi.org/10.3847/1538-4357/836/2/185)

Taylor, A. R., Stil, J. M., & Sunstrum, C. 2009, ApJ, 702, 1230, doi: [10.1088/0004-637X/702/2/1230](https://doi.org/10.1088/0004-637X/702/2/1230)

Vallee, J. P. 1990, AJ, 99, 459, doi: [10.1086/115343](https://doi.org/10.1086/115343)

van Weeren, R. J., Andrade-Santos, F., Dawson, W. A., et al. 2017, Nature Astronomy, 1, 0005, doi: [10.1038/s41550-016-0005](https://doi.org/10.1038/s41550-016-0005)

Vargas, C. J., Mora-Partiarroyo, S. C., Schmidt, P., et al. 2018, ApJ, 853, 128, doi: [10.3847/1538-4357/aaa47f](https://doi.org/10.3847/1538-4357/aaa47f)

Virtanen, P., Gommers, R., Oliphant, T. E., et al. 2020, Nature Medicine, 17, 261, doi: [10.1038/s41592-019-0686-2](https://doi.org/10.1038/s41592-019-0686-2)

Vollmer, B., Beck, R., Kenney, J. D. P., & van Gorkom, J. H. 2004, AJ, 127, 3375, doi: [10.1086/420802](https://doi.org/10.1086/420802)

Vollmer, B., Braine, J., Pappalardo, C., & Hily-Blant, P. 2008a, A&A, 491, 455, doi: [10.1051/0004-6361:200810432](https://doi.org/10.1051/0004-6361:200810432)

Vollmer, B., Soida, M., Beck, R., et al. 2013, A&A, 553, A116, doi: [10.1051/0004-6361/201321163](https://doi.org/10.1051/0004-6361/201321163)

Vollmer, B., Soida, M., Beck, R., et al. 2007, A&A, 464, L37, doi: [10.1051/0004-6361:20066980](https://doi.org/10.1051/0004-6361:20066980)

Vollmer, B., Soida, M., Chung, A., et al. 2010, A&A, 512, A36, doi: [10.1051/0004-6361/200913591](https://doi.org/10.1051/0004-6361/200913591)

Vollmer, B., Soida, M., Chung, A., et al. 2008b, A&A, 483, 89, doi: [10.1051/0004-6361:20078139](https://doi.org/10.1051/0004-6361:20078139)

Vollmer, B., Soida, M., Chung, A., et al. 2006, A&A, 453, 883, doi: [10.1051/0004-6361:20064954](https://doi.org/10.1051/0004-6361:20064954)

Vulcani, B., Poggianti, B. M., Gullieuszik, M., et al. 2018, ApJL, 866, L25, doi: [10.3847/2041-8213/aae68b](https://doi.org/10.3847/2041-8213/aae68b)

Vulcani, B., Fritz, J., Poggianti, B. M., et al. 2020a, ApJ, 892, 146, doi: [10.3847/1538-4357/ab7bdd](https://doi.org/10.3847/1538-4357/ab7bdd)

Vulcani, B., Poggianti, B. M., Tonnesen, S., et al. 2020b, *ApJ*, 899, 98, doi: [10.3847/1538-4357/aba4ae](https://doi.org/10.3847/1538-4357/aba4ae)

Wang, J., Staveley-Smith, L., Westmeier, T., et al. 2021, *ApJ*, 915, 70, doi: [10.3847/1538-4357/abfc52](https://doi.org/10.3847/1538-4357/abfc52)

Watts, A. B., Cortese, L., Catinella, B., et al. 2024, *MNRAS*, 530, 1968, doi: [10.1093/mnras/stae898](https://doi.org/10.1093/mnras/stae898)